



HAL
open science

Implications of recently derived thermodynamic data and specific ionic interaction theory parameters for $(\text{Mg}/\text{Ca})_n\text{UO}_2(\text{CO}_3)_{3^{(4-2n)-}}$ complexes on the predominance of the $\text{Mg}^{2+}-\text{Ca}^{2+}-\text{UO}_2^{2+}-\text{OH}^--\text{CO}_3^{2--}$ systems, and application to natural and legacy-mine waters

Chengming Shang, Nathalie Coreau, Nathalie Macé, Michael Descostes,
Pascal E. Reiller

► **To cite this version:**

Chengming Shang, Nathalie Coreau, Nathalie Macé, Michael Descostes, Pascal E. Reiller. Implications of recently derived thermodynamic data and specific ionic interaction theory parameters for $(\text{Mg}/\text{Ca})_n\text{UO}_2(\text{CO}_3)_{3^{(4-2n)-}}$ complexes on the predominance of the $\text{Mg}^{2+}-\text{Ca}^{2+}-\text{UO}_2^{2+}-\text{OH}^--\text{CO}_3^{2--}$ systems, and application to natural and legacy-mine waters. *Science of the Total Environment*, 2023, 858 (Part 2), pp.159927. 10.1016/j.scitotenv.2022.159927. cea-03852799

HAL Id: cea-03852799

<https://cea.hal.science/cea-03852799>

Submitted on 15 Nov 2022

HAL is a multi-disciplinary open access archive for the deposit and dissemination of scientific research documents, whether they are published or not. The documents may come from teaching and research institutions in France or abroad, or from public or private research centers.

L'archive ouverte pluridisciplinaire **HAL**, est destinée au dépôt et à la diffusion de documents scientifiques de niveau recherche, publiés ou non, émanant des établissements d'enseignement et de recherche français ou étrangers, des laboratoires publics ou privés.

Implications of recently derived thermodynamic data and specific ionic interaction theory parameters for $(\text{Mg}/\text{Ca})_n\text{UO}_2(\text{CO}_3)_3^{(4-2n)-}$ complexes on the predominance of the $\text{Mg}^{2+}-\text{Ca}^{2+}-\text{UO}_2^{2+}-\text{OH}^{-}-\text{CO}_3^{2-}$ systems, and application to natural and legacy-mine waters.

Chengming Shang,^{a,†} Nathalie Coreau,^b Nathalie Macé,^b Michael Descostes,^{c,d} and Pascal E. Reiller^{a,*}

a Université Paris-Saclay, CEA, Service d'Études Analytiques et de Réactivité des Surfaces (SEARS), F-91191 Gif-sur-Yvette CEDEX, France.

b Université Paris-Saclay, CEA, Service d'Études du Comportement des Radionucléides (SECR), F-91191 Gif-sur-Yvette CEDEX, France.

c ORANO Mining, Environmental R&D Department, 125 Avenue de Paris, 92330, Châtillon, France.

d PSL University/Mines ParisTech, Centre de Géosciences, 35 rue Saint-Honoré, 77305, Fontainebleau, France.

Corresponding author's e-mail: pascal.reiller@cea.fr.

† present address: Karlsruhe Institute of Technology, Institute for Nuclear Waste Disposal, P.O. Box 3640, 76021, Karlsruhe, Germany

Abstract

The formation of alkaline earth(II)triscarbonatouranyl(VI) ($\text{Ae}_n\text{UO}_2(\text{CO}_3)_3^{(4-2n)-}$) species that have been evidenced both in laboratory and in-field studies, is important from slightly acidic pH up to near degraded cementitious in carbonated waters. They are also showing distinctive luminescence properties with a hypsochromic shift relative to UO_2^{2+} . The conditions of pH, activities of alkaline earth(II) free ions (mostly Mg^{2+} and Ca^{2+}) and carbonate ions (HCO_3^{-}) can be predicted from the thermodynamic functions and constants. The predictive validity of the

activity of major alkaline ions (mostly Na^+) is determined from the models used to describe the ionic strength compartment of these species, particularly using coefficients from the specific ion interaction theory (SIT). The stability domains of these species are better defined as a function of the activity of the constituents, and applied to natural waters. In this work, using recently obtained complete thermodynamic data and SIT coefficients, we will draw the stability domains of the $\text{Ae}_n\text{UO}_2(\text{CO}_3)_3^{(4-2n)-}$ species in combinations of activities of H^+ , HCO_3^- , Mg^{2+} , Ca^{2+} , and Na^+ for a wide selection of water compositions from the literature. Water samples were collected near a French mining legacy-site (Site du Bosc, Lodève, France). After determining the major ion compositions, we will verify that the luminescence signal of uranium is in agreement with the predicted speciation in the stability domains.

1. Introduction

Uranium is a metal of major concern for the safety assessment and environmental monitoring of every nuclear cycle aspect: from mining operation to underground geological disposal of radioactive waste. Since the mid 1990's, and the seminal works from Bernhard et al. (1996, 1998; 2001), the formation of triscarbonatouranyl(VI) complexes with alkaline earth(II) (Ae(II)) $\text{Ae}_n\text{UO}_2(\text{CO}_3)_3^{(4-2n)-}$ complexes — issued from the formation of the liebigite family phases $\text{Alk}_{2n}\text{Ae}_m\text{Ae}'_{(2-n-m)}\text{UO}_2(\text{CO}_3)_3 \cdot x\text{H}_2\text{O}$, where Alk is an alkaline metal, Ae and Ae' are alkaline earth metals (Alwan and Williams, 1980; Kubatko et al., 2005; Lee et al., 2019; Li and Burns, 2001; Mereiter, 1982; Meyrowitz, 1954; Meyrowitz et al., 1963; O'Brien and Williams, 1983; Smith, 1848, 1851) — has been the object of physical (Kelly et al., 2007), chemical (Endrizzi et al., 2016; Kelly et al., 2005), and theoretical (Li et al., 2017; Oher et al., 2020; Priest et al., 2016) studies. Their presence and impact on uranium adsorption and transport have also been particularly studied (Baik et al., 2015; Endrizzi et al., 2016; Fox et al., 2006; Hennig et al., 2020; Maloubier et al., 2015; Montavon et al., 2022; Nair and Merkel, 2011; Osman et al., 2013; Prat et al., 2009; Stewart et al., 2010; Stockmann et al., 2021; Wang et al., 2004).

During the past 26 years, the thermodynamic constants and functions of these complexes have been studied (Bernhard et al., 1996; Bernhard et al., 2001; Dong and Brooks, 2006, 2008; Endrizzi and Rao, 2014; Geipel et al., 2008; Jo et al., 2019a; Jo et al., 2019b; Kalmykov and Choppin, 2000; Lee and Yun, 2013; Lee et al., 2017; Maia et al., 2021; Shang and Reiller, 2020; Shang et al., 2020; Shang and Reiller, 2021a, b). Neither these species nor the phases have been selected in the widely recognized selection commissioned by the Thermochemical Data Base project from the Nuclear Energy Agency of the Organization for the Economic Cooperation and Development (NEA-OECD) after their discovery (Guillaumont et al., 2003). However, the thermodynamic constants (stepwise $\log_{10}K^\circ$, or cumulative $\log_{10}\beta^\circ$), functions of reaction ($\Delta_r G^\circ_m$, $\Delta_r H^\circ_m$, $\Delta_r S^\circ_m$, $\Delta_r C_p^\circ_m$), and formation ($\Delta_f G^\circ_m$, $\Delta_f H^\circ_m$, $S^\circ_{f,m}$, $C_p^\circ_{f,m}$) at the standard state have been recently selected in the latter update of this review (Grenthe et al., 2020). Due to the lack of studies proposing $\log_{10}K$ or $\log_{10}\beta$ values at varying ionic strength, the selected data did not include the important specific ion interaction coefficients $\varepsilon(\text{Ae}_n\text{UO}_2(\text{CO}_3)_3^{(4-2n)-}, \text{Na}^+\text{X}^-)$ obtained from the extrapolation of thermodynamic constants to infinite dilution, and are necessary for a back-extrapolation to actual ionic strength of natural media — see annex B in NEA-OECD selections (Grenthe et al., 2020; Guillaumont et al., 2003).

To help better defining the predominance domain of these complexes, Reiller and Descostes (2020) proposed predominance activity diagrams — $\log_{10} a(\text{SO}_4^{2-})$ -pH domains at constant $\log_{10} a(\text{Ca}^{2+})$, $\log_{10} a(\text{Mg}^{2+})$, and $P(\text{CO}_2)$ — of the $\text{Ae}_n\text{UO}_2(\text{CO}_3)_3^{(4-2n)-}$ complexes, based on speciation calculation of water compositions relevant of uranium mining activities and of other varying occurrences. The values of formation constants for $\text{Ca}_n\text{UO}_2(\text{CO}_3)_3^{(4-2n)-}$ were taken from Dong and Brooks (2006) — as well as those for $\text{SrUO}_2(\text{CO}_3)_3^{2-}$ and $\text{Ba}_n\text{UO}_2(\text{CO}_3)_3^{(4-2n)-}$ —, and the one of $\text{MgUO}_2(\text{CO}_3)_3^{2-}$ was chosen from Dong and Brooks (2008). In chemical modelling, the evolution of $\log_{10}\beta(\text{Ae}_n\text{UO}_2(\text{CO}_3)_3^{(4-2n)-})$ vs. ionic strength is important to be specified as the final speciation results can show significant differences due to different choices of activity

corrections (Shang and Reiller, 2020, 2021a). However, the determination of specific ion interaction coefficients ε for these ternary complexes — particularly $(\text{Mg}/\text{Ca})_n\text{UO}_2(\text{CO}_3)_3^{(4-2n)-}$ complexes — did not receive sufficient attention and only the value of $\varepsilon(\text{MgUO}_2(\text{CO}_3)_3^{2-}, \text{Na}^+)$ was reported by Dong and Brooks (2008) at the cut-off time of the review from Grenthe et al. (2020). Therefore, $\varepsilon(\text{MgUO}_2(\text{CO}_3)_3^{2-}, \text{Na}^+) = -3.2 \text{ kg}_w \text{ mol}^{-1}$, based on Dong and Brooks (2008), and $\varepsilon(\text{Ca}_n\text{UO}_2(\text{CO}_3)_3^{(4-2n)-}, \text{Na}^+) = 0$, because of non-availability — with the exception of the works from Kalmykov and Choppin (2000) —, were taken in the theoretical speciation calculations in Reiller and Descostes (2020), which was published before Grenthe et al. (2020) was effectively published.

Since then, a series of standard state thermodynamic constants and functions, accompanied by $\varepsilon(\text{Ae}_n\text{UO}_2(\text{CO}_3)_3^{(4-2n)-}, \text{Na}^+\text{X}^-)$ values in NaCl and NaClO₄, have been proposed (Shang and Reiller, 2020; Shang et al., 2020; Shang and Reiller, 2021a, b). It seems important to gather these data and precise the different conditions under which these complexes are predominant for the speciation of uranium in different media, within the nuclear fuel cycle, but also beyond, as variation of natural concentrations of uranium could as well be a concern for public health (Braz et al., 2021; Coyte et al., 2018; Prat et al., 2009). Moreover, sea- and ocean-waters contain a total high mass of uranium, even at global trace concentration (OECD-IAEA, 2014).

The main objective of this work was to examine the main species in natural water compositions linked to radioactive waste management (RWM), uranium mining activities, and of other more general interests related to natural uranium with the recently determined thermodynamic data and ε values for $(\text{Mg}/\text{Ca})_n\text{UO}_2(\text{CO}_3)_3^{(4-2n)-}$ complexes obtained in previous studies (Shang and Reiller, 2020; Shang et al., 2020; Shang and Reiller, 2021a, b). The speciation of the different water compositions was calculated using either PHREEQC/PHREEPLOT (Kinniburgh and Cooper, 2011; Parkhurst and Appelo, 1999, 2013), and the Thermochemie 10a or 9b database files, respectively (<https://www.thermochimie->

tdb.com/) (Giffaut et al., 2014; Grivé et al., 2015). The $\log_{10}\beta^\circ$, and ε values in NaCl medium, from Shang and Reiller (2020, 2021a) for $(\text{Mg,Ca})_n\text{UO}_2(\text{CO}_3)_3^{(4-2n)-}$ were implemented in the input files — see Table S1 of the SI. The speciation of uranium as well as the calculated activities of H^+ , HCO_3^- , Mg^{2+} , Ca^{2+} , and Na^+ were retrieved. These activities are the ones who are supposed to control primarily the formation of these complexes as they either impact through the mass action law or through the ionic strength dependence. From these results, activity diagrams were plotted using PHREEPLOT (Kinniburgh and Cooper, 2011) in order to have a common representation under which all the parameters and complexes can be represented.

Once this representation was obtained, an application to actual waters collected before treatment in the mining legacy-site around Lodève in France (site du Bosc) was conducted taking advantages of the luminescent properties of the $(\text{Mg/Ca})_n\text{UO}_2(\text{CO}_3)_3^{(4-2n)-}$ complexes (Bernhard et al., 1996, 1998; Bernhard et al., 2001; Kalmykov and Choppin, 2000; Lee and Yun, 2013; Shang and Reiller, 2020; Shang et al., 2020; Shang and Reiller, 2021a). The composition of the collected waters major ions was determined, and the uranium concentration and speciation was determined using time-resolved laser-induced fluorescence spectroscopy (TRLFS) and calculated using PHREEQC (Parkhurst and Appelo, 1999, 2013). Luminescence spectra and decay-time evolution of uranium in the collected waters were compared to a known synthetic solution, in order to confirm the presence and calculated speciation of the $(\text{Mg/Ca})_n\text{UO}_2(\text{CO}_3)_3^{(4-2n)-}$ complexes in the selected waters.

2. Materials and Methods

2.1. Time-resolved laser-induced luminescence

TRLFS is versatile technique, which allows both measuring total concentration of uranium (Moulin et al., 1990; Reiller et al., 1994), and obtaining information on its chemical

environment (Oher et al., 2020). The TRLFS apparatus has been extensively described in previous works (Shang and Reiller, 2020; Shang et al., 2020; Shang and Reiller, 2021a, b). It consists of a 355 nm Nd:YAG pulsed laser (10 Hz, Surelite, Continuum, USA) delivering about 170 mJ during a 5 ns pulse. The adjustable excitation wavelength chosen from the optical parametric oscillator (OPO, Horizon, Continuum, USA) is $\lambda_{\text{exc}} = 450 \text{ nm}$ (*ca.* 20 mJ) in order to balance between the U(VI) quantum yield and the efficacy of the OPO; the measures were done at a delay D after the laser pulse between 25 and 215 ns, during a gate width W of 1 μs . The spectra were recorded using the 300 lines mm^{-1} grating of a monochromator spectrometer (Acton).

For uranium concentration determination in TRLFS the most convenient medium is 5% wt. H_3PO_4 (Moulin et al., 1990; Reiller et al., 1994). A 2 mL aliquot of the site du Bosc waters was weighed in a quartz cuvette (QS101, Suprasil, Hellma Analytics), and the needed mass of concentrated H_3PO_4 (85 wt. %, Sigma-Aldrich) to attain 5% wt., or $0.75 \text{ mol kg}_w^{-1}$, was added. The concentration was determined relative to four sub-standard solutions in 5% H_3PO_4 prepared by weighing from the initial stock U(VI) solution of known concentration prepared from previous studies (Shang and Reiller, 2020, 2021a). The recorded spectra at $D = 25 \text{ ns}$ with fixed gate width $W = 1 \mu\text{s}$ were integrated over the wavelength span from 415 nm to 615 nm to estimate the luminescence intensity. A graph of luminescence intensity *vs.* U concentration is plotted for the four standard solutions, as shown in Figure S1 of the electronic supplemental information ESI. For luminescence and decay-time measurements of uranium in the site du Bosc waters, around 2 mL aliquots of the site du Bosc water were used in quartz cuvettes without any modification.

A solution identical to the one analyzed in Oher et al. (2020) containing 100% $\text{CaUO}_2(\text{CO}_3)_3^{2-}$ was also measured — $50 \mu\text{mol kg}_w^{-1}$ U. It is worthy to recall that the band

positions of $\text{Ca}_n\text{UO}_2(\text{CO}_3)_3^{(4-2n)-}$ cannot be distinguished using the 300 lines mm^{-1} grating (Oher et al., 2020).

2.2. Ionic chromatography

The ion chromatographic system was a Metrohm (CI 850), equipped for anions with a Metrosep A Supp 4/5 Guard pre-column, a Metrosep A Supp 7 150/4.0 column, an eluent asup7 — 3.6 mM Na_2CO_3 at 0.7 mL min^{-1} ; for the cations a Metrosep C 4 Guard/4.0 pre-column, a Metrosep C 4 -150/C4 column, an eluent C4 — HNO_3 3.5 mM, at 0.9 mL min^{-1} .

2.3. Total Organic Carbon Analysis

The total organic carbon (TOC) determinations were performed with VARIOTOC cube analyzer (Elementar). The total inorganic carbon (TIC) is measured by mixing in the TIC-reactor 0.1 mL of the sample with 0.5 mL of H_3PO_4 diluted solution prepared from a concentrated commercial one (85%, Merck). The total carbon (TC) is obtained by a Pt-catalytic combustion at 850°C of samples. After TIC and TC reactions, $\text{CO}_2(\text{g})$ produced is measured by IR. The TOC is obtained by the difference between TC and TIC. When uncertainties on TOC determination are considered too high, one can pre-acidify the sample prior the carbon determination. In that case, TIC is negligible and TOC corresponds directly to the TC determination. The calibration was done using standards solutions prepared by mixing with Milli-Q water (Millipore, 18.2 $\text{M}\Omega\cdot\text{cm}$, $\text{TOC} = 5\text{ppbc}$) potassium hydrogen phthalate ($\text{K}_2\text{H}_4\text{O}_4\text{C}_8$, Elementar S35.00-0151) in TOC (0.08 to 1.73 $\text{mmol}_\text{C L}^{-1}$) and anhydrous sodium carbonate (Na_2CO_3 , Elementar S35.00-0152) in TIC (0.04 to 0.82 $\text{mmol}_\text{C L}^{-1}$). The injected volume was 0.1 mL and each sample was replicated 3 times. A blank consisted in Milli-Q water was inserted between each sample to measure the background in TIC and TC.

2.4. UV-Visible spectroscopy

The UV-Visible (UV-Vis) spectra were obtained using a Shimadzu UV-3150 double beam spectrophotometer in the 200-400 wavelength range. Samples were measured in the fluorescence quartz cuvette (cf. § 2.1), using pure water as reference.

2.5. pH measurement

The pH-measurement procedure has already been described in details in Shang and Reiller (2020, 2021a). With use of the Na^+ and Cl^- concentration, the potential measured by the combined-glass (Mettler Toledo, USA) pH electrode was converted to a pH value.

2.6. Description of studied water compositions

2.6.1. Data from literature

The chemical composition of natural water is a result of the physical, chemical, and biochemical processes that occur in the atmosphere-soil-rock water system. A wide range of chemical elements can dissolve in natural waters due to interactions with the atmosphere, the surrounding environment, soil, and bedrock. In particular, the rock-mineral solubility has a decisive influence on the chemical composition of natural water. Type and amount of major, secondary, and minor elements, are considerably variable and reflect the nature and effects of geochemical processes on groundwater composition.

To build our representations in activity diagrams, a number of natural water compositions were collected from literature. The measurement of the geochemical parameters — *i.e.* pH value, redox potential, salinity, alkalinity, temperature, *etc.* — and important characteristics for speciation modelling were taken for each collected sample. The selected water conditions cover those reported for:

- (a) waters in underground research laboratories (URL) for radioactive waste management (RWM), *e.g.*, clay porewaters — Boom clay in Belgium (De Craen et al., 2004), Callovo-Oxfordian (Gaucher et al., 2009) and Tournemire (Beaucaire et al., 2008) clays in France, and Mont-Terri clay in Switzerland (Courdouan Merz, 2008; Thury and Bossart, 1999) — and granitic groundwaters — Äspö site, Forsmark and Laxemar-Simpevarp areas in Sweden (Emrén et al., 1999; Laaksoharju et al., 2008; Tullborg et al., 2017);
- (b) groundwaters in acid In Situ Recovery (ISR) contexts from ORANO mining sites — see Reiller and Descostes (2020) and references therein —; in Al-Batin Alluvial Fan, Southern Iraq (Alkinani et al., 2016); and in the Lodève basin, France (Beaucaire and Toulhoat, 1987);
- (c) waters crossing the Cigar Lake mining site, Saskatchewan, Canada (Toulhoat and Beaucaire, 1993); and in the Oklo uranium deposit area (Gurban et al., 2003; Salas and Ayora, 2004);
- (d) well waters as local sources of drinking sources in Finland (Prat et al., 2009); around the Semipalatinsk Nuclear Test Site in Kazakhstan (Yamamoto et al., 2010); and near-surface Canadian aquitards considered as underlying groundwater (Hendry and Wassenaar, 2000; Ranville et al., 2007);
- (e) waters sampled upstream, downstream, and within uranium mining sites, *e.g.*, Cluff Lake in Canada (von Gunten et al., 2018), and Lac Saint-Clément in France (Stetten et al., 2018);
- (f) standard seawater (Millero et al., 2008), as source of uranium (Beccia et al., 2017; Endrizzi et al., 2016; Leggett et al., 2016; Maloubier et al., 2015), and evolution along the Scheldt estuary (Belgium) (Smolřková et al., 2022);
- (g) selected waters compositions issued from the general dataset generated through the European project FOREGS (Forum of European Geological Surveys, <http://weppi.gtk.fi/publ/foregsatlas/>), which uranium speciation were analyzed in Lartigue et al. (2020).

Generally, these natural waters are dominated by Na^+ , Ca^{2+} , Mg^{2+} , K^+ , Cl^- , NO_3^- , HCO_3^- , CO_3^{2-} , and SO_4^{2-} that may be attributed to the chemical weathering process and the leaching of minerals. Among these ions, chloride concentration is the most suitable parameter to describe water salinity because of its high solubility. The concentration of uranium in the collected samples highly depends on the sampling regions. In most natural waters, uranium concentration is between 4.2×10^{-10} M and 4.2×10^{-9} M (Osmond et al., 1983). In Europe, the average uranium concentration in continental surface water is estimated to be *ca.* $0.3 \mu\text{g L}^{-1}$ ($\approx 1.26 \times 10^{-9}$ M) while it is *ca.* $0.5 \mu\text{g L}^{-1}$ ($\approx 2.1 \times 10^{-9}$ M) worldwide (De Vos et al., 2005). In river waters, it can extend over four orders of magnitude with average content from 0.02 to $6 \mu\text{g L}^{-1}$ ($\approx 8.40 \times 10^{-11}$ to 2.52×10^{-8} M) (Bonin and Blanc, 2001). In France, the uranium concentration in river waters is about $0.44 \mu\text{g L}^{-1}$ ($\approx 1.85 \times 10^{-9}$ M) in sedimentary areas, and expected to be slightly lower than $0.15 \mu\text{g L}^{-1}$ in the Hercynian shelf and Alpine areas (Salpeteur and Angel, 2010). In extreme cases, concentration up to $3400 \mu\text{g L}^{-1}$ have been measured in drinking waters from drilled wells (Prat et al., 2009). A wider view on uranium concentration in e.g. river waters can be found in Lartigue et al. (2020). However, in mines the uranium concentration in groundwater can range from 0.063 to $1.68 \mu\text{M}$ (Fix, 1956).

2.6.2. Description of calculations of uranium speciation in the selected samples

The selection of the software, the database file and activity correction would have a particular effect on the simulation results (Emrén et al., 1999). The calculations were performed using the PHREEQC version 3.4.0.14000 (Parkhurst and Appelo, 1999, 2013) for the speciation calculation and Phreeplot 1.0 (Kinniburgh and Cooper, 2004; Kinniburgh and Cooper, 2011) for the activity diagrams. According to the SIT definition in PHREEQC, activity correction adopted in this work, the formation constants at infinite dilution $\log_{10}\beta^\circ$, the thermodynamic functions $\Delta_f H_m^\circ$ and SIT parameters, specific ion interaction coefficients $\varepsilon((\text{Mg}/\text{Ca})_n\text{UO}_2(\text{CO}_3)_3^{(4-2n)-}, \text{Na}^+\text{Cl}^-)$ complexes from Shang and Reiller (2020, 2021a), were

implemented in the input files, and the Thermochemie 10a database (Giffaut et al., 2014; Grivé et al., 2015) was used. The reader is recalled that more recent versions of Thermochemie (10d and 11a) are available for download. These latter versions will only be partly used in this work, as they were made available after the end of this project. A discussion on the data selection will be developed in the following (cf. § 3.1).

2.6.3. Water from the site du Bosc (Lodève, France)

The water coming out of the Site du Bosc (Lodève, Hérault, France) must be treated in order to follow the French legislation and orders from local authorities. The routine treatment is done using an ion-exchange resin (Drozdak et al., 2016a; Morin, 2005). Before treatment (pH *ca.* 8.2, hereafter “untreated water”), the waters are filtered at 0.45 μm and then acidified using H_2SO_4 (pH *ca.* 6.5, hereafter “treated water”) in order to help further dissolving possible colloidal carbonate particles. The buffer capacities of these carbonate particles induce an increase of the pH value close to the original one. The modification of alkaline earth ions concentration is also in question.

The untreated and treated samples were sent to the CEA laboratory. The water samples undertook no further treatment in order to stay as close as possible to the actual treatment situation. The composition of Le Bosc site has been investigated elsewhere (Drozdak et al., 2016a; Drozdak et al., 2016b), but either exact pH or total U or Na amounts are missing. The water composition was then analyzed in ion chromatography coupled to ICP-MS for major ions, and TRLFS for uranium. With this information, it is possible to perform a theoretical speciation calculation and then compare with the luminescence of the dominant species experimentally observed by TRLFS.

3. Results and Discussions

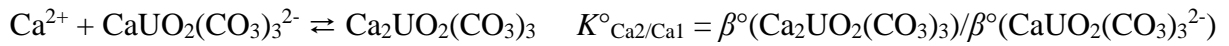
3.1. Differences in speciation of $(Mg,Ca)_nUO_2(CO_3)_3^{(4-2n)-}$ between thermodynamic data from different origins

Apart from the results of Shang & Reiller (2020, 2021a, b), the $Ae_nUO_2(CO_3)_3^{(4-2n)-}$ species were recently included in the NEA-OECD selections (Grenthe et al., 2020) — with no selection of ϵ values —, and in the versions of Thermochemie 10 (a and d) and 11a. Very recently, Jo et al. (2022) reviewed more recent data on the system. Thermochemie 10d and 11a, and Jo et al. (2022) were available late in the advancement of this project and will only be considered in this section. These data will not be considered in the following. The $\log_{10}\beta_{n.1.3}^\circ$ from Dong and Brooks (2006) (Ca) and Lee et al. (2017) (Mg, not present in version 10a), and the ϵ values from like-charged analogy — with a typographic error on $\epsilon(MgUO_2(CO_3)_3^{2-}, Na^+) = -0.2 \text{ kg}_w \text{ mol}^{-1}$ instead of $-0.02 \text{ kg}_w \text{ mol}^{-1}$ announced in analogy with $\epsilon(UO_2(CO_3)_3^{2-}, Na^+)$ (<https://www.thermochemie-tdb.com/pages/view.php>) and corrected in version 11a —, were chosen in Thermochemie 10. In Thermochemie 11a, the $\log_{10}\beta_{n.1.3}^\circ$ values from Grenthe et al. (2020), and the ϵ values from like-charged analogy were chosen.

The impact of the choice of the data is shown in Figure 1. Theoretical speciation calculations of a solution with $C_U = 10^{-9} \text{ mol kg}_w^{-1}$ — to minimize formation of $(UO_2)_2CO_3(OH)_3^-$ —, $C_{Mg} = C_{Ca} = 10^{-2} \text{ mol kg}_w^{-1}$, $[NaCl] = 0.5 \text{ mol kg}_w^{-1}$ — to maximize ionic strength effects —, and $P(CO_2) = 10^{-3.5} \text{ atm}$ is plotted in the pH range 6-10 fixed by $MgCa(OH)_4$, and where dolomite ($MgCa(CO_3)_2$) is required to precipitate. It can be seen that the predominance of the $Ae_nUO_2(CO_3)_3^{(4-2n)-}$ complexes are different in the three calculations. $CaUO_2(CO_3)_3^{2-}$ is clearly dominant at pH 7 to 9, when $Ca_2UO_2(CO_3)_3(aq)$ is dominant under the other two situations. Here, the differences mainly come for the hypotheses on the ϵ values: explicit from experiments

in Shang and Reiller (2020) in Figure 1a, and either considered nil in Figure 1b (Grenthe et al., 2020), or from liked-charged analogy in Thermochimie 10d and 11a.

The relative affinity of the different reactions can be estimated calculating the stepwise reactions for the cumulative reactions in Table S1 of the SI.



The calculated relative affinity under standard conditions are $K^\circ(\text{CaUO}_2(\text{CO}_3)_3^{2-})/K^\circ(\text{Ca}_2\text{UO}_2(\text{CO}_3)_3) = 117$ (Shang and Reiller, 2020, 2021a), 23 (Grenthe et al. (2020), and Thermochimie 11a), and 66 (Thermochimie 10a and 10d). Accounting for ionic strength at 0.5 mol kg⁻¹ NaCl, $K^{0.5\text{m}}(\text{CaUO}_2(\text{CO}_3)_3^{2-})/K^{0.5\text{m}}(\text{Ca}_2\text{UO}_2(\text{CO}_3)_3) = 5.0$ (Shang and Reiller, 2020), 0.9 (Grenthe et al. (2020), and Thermochimie 11a), and 2.6 (Thermochimie 10a) and 2.7 (Thermochimie 10d). The relative affinity for $K^\circ(\text{CaUO}_2(\text{CO}_3)_3^{2-})/K^\circ(\text{MgUO}_2(\text{CO}_3)_3^{2-}) = 6.3$ (Shang and Reiller, 2020, 2021a), 6.3 (Grenthe et al. (2020), and Thermochimie 11a), and 24.0 (Thermochimie 10d) — $\text{MgUO}_2(\text{CO}_3)_3^{2-}$ was not present in Thermochimie 10a. At ionic strength 0.5 mol kg⁻¹ NaCl, $K^{0.5\text{m}}(\text{CaUO}_2(\text{CO}_3)_3^{2-})/K^{0.5\text{m}}(\text{MgUO}_2(\text{CO}_3)_3^{2-}) = 4.7$ (Shang and Reiller, 2020, 2021a), 5.9 (Grenthe et al. (2020), and Thermochimie 11a), and 22.6 (Thermochimie 10d) — typographic error in $\varepsilon(\text{MgUO}_2(\text{CO}_3)_3^{2-}, \text{Na}^+)$ is corrected.

Because of the higher relative affinity for $\text{Ca}_n\text{UO}_2(\text{CO}_3)_3^{(4-2n)-}$ compared to $\text{MgUO}_2(\text{CO}_3)_3^{2-}$, the proportion of the latter complex is lower in the three hypothesis. Percentage of $\text{MgUO}_2(\text{CO}_3)_3^{2-}$ is then higher in Figure 1a than in Figure 1b or 1c as the $\varepsilon(\text{MgUO}_2(\text{CO}_3)_3^{2-}, \text{Na}^+\text{Cl}^-)$ determined in Shang and Reiller (2021a), is either not nil — as in

Grenthe et al. (2020) — or higher than the like-charged hypothesis in Thermochemie 10d and 11a. The relative affinity $K^\circ(\text{CaUO}_2(\text{CO}_3)_3^{2-})/K^\circ(\text{MgUO}_2(\text{CO}_3)_3^{2-})$ of Ca^{2+} for $\text{UO}_2(\text{CO}_3)_3^{4-}$ is lower than Mg^{2+} and the proportion of $\text{MgUO}_2(\text{CO}_3)_3^{2-}$ is then higher in Shang and Reiller (2020, 2021a) (Figure 1a) compared to Thermochemie 10d (Figure 1c).

The data from Shang and Reiller (2020, 2021a, b) being the only one issued from consistent sets of experimental data, they will be used in the following.

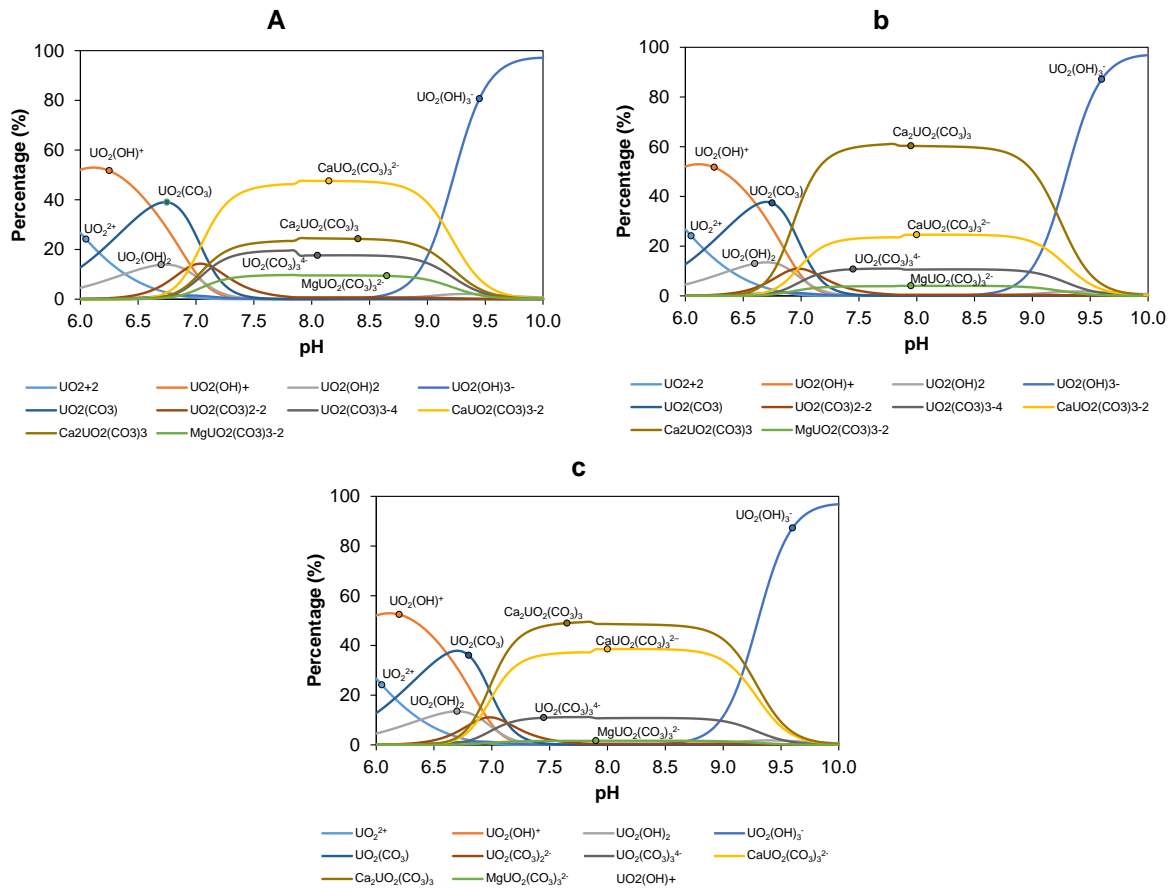
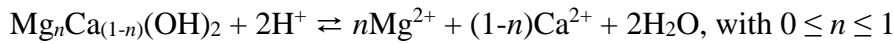


Figure 1. Theoretical speciation of a solution $C_U = 10^{-9} \text{ mol kg}_w^{-1}$, $C_{Mg} = C_{Ca} = 10^{-2} \text{ mol kg}_w^{-1}$, $[\text{NaCl}] = 0.5 \text{ mol kg}_w^{-1}$, and $P(\text{CO}_2) = 10^{-3.5} \text{ atm}$, pH fixed by $\text{Mg}(\text{OH})_2$ - $\text{Ca}(\text{OH})_2$ and dolomite is required to precipitate, using thermodynamic and SIT data from Shang and Reiller (2020) (a), Grenthe et al. (2020) — with dolomite from Robie and Hemingway (1995) — (b), and Thermochimie 10d database file (<https://www.thermochimie-tdb.com/>) with $\epsilon(\text{MgUO}_2(\text{CO}_3)_3^{2-}, \text{Na}^+)$ corrected to $-0.02 \text{ kg}_w \text{ mol}^{-1}$ (c); the discontinuity at pH 7.8 is due to the dolomite precipitation.

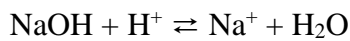
3.2. Description of activity predominance diagrams

Figure 2 illustrates the evolution of predominance diagrams obtained using PHREEPLOT (Kinniburgh and Cooper, 2011) for the system Ca^{2+} - $\text{U}(\text{IV}/\text{VI})$ - Na^+ - Cl^- - OH^- - HCO_3^- - $\text{H}_2\text{O}(\text{l})$ as a function of partial pressure of oxygen. The activity diagrams $\log_{10}(a(\text{HCO}_3^-) a(\text{H}^+))$ vs. $\log_{10}(a(\text{Mg}^{2+})^{0.5} a(\text{Ca}^{2+})^{0.5}/a(\text{H}^+)^2)$ have been chosen for the presentation due to the number of

variables affecting this system. It allows representing the variation of H_2CO_3 and $(\text{Mg-Ca})_{0.5}(\text{OH})_2$. These equilibria can be written in a general form as follows.



In the following, the influence of Na^+ and pH will be represented by $\log_{10}(a(\text{Na}^+)/a(\text{H}^+))$ and the following equilibrium.



The calculations were conducted at fixed uranium concentration of $10^{-8} \text{ mol kg}_w^{-1}$ at $I_m = 0.1 \text{ mol kg}_w^{-1}$ NaCl with $P(\text{O}_2)$ varying from 10^{-73} to 10^{-51} atm — or $\text{pO}_2 = -\log_{10} P(\text{O}_2)$, varying from 73 to 51, which covers a wide range of actual underground research laboratory for the radioactive waste management — *e.g.*, of $\text{pO}_2 = 73$, *ca.* the value for Äspö site in Sweden, to $\text{pO}_2 = 67$, *ca.* the value for Callovo-Oxfordian site in France. One can observe that the partial pressure of oxygen has a significant impact on the aqueous speciation of uranium as well as its oxidation state. Because of the redox sensitivity of uranium, the oxidation-reduction reactions are very important in the assessment of uranium mobility. Uranium exists as $\text{U}(\text{OH})_4(\text{aq})$, under its +IV redox state, at low $P(\text{O}_2)$ ($\text{pO}_2 = 73$ and 67) and $\log_{10}(a(\text{HCO}_3^-) a(\text{H}^+))$ at the expenses of $\text{Ca}_n\text{UO}_2(\text{CO}_3)_3^{(4-2n)-}$ complexes. With increasing $P(\text{O}_2)$, the formation of Ca-UO₂-CO₃ ternary complexes takes place within larger range at higher $\log_{10}(a(\text{HCO}_3^-) a(\text{H}^+))$ and $\log_{10}(a(\text{Mg}^{2+})^{0.5} a(\text{Ca}^{2+})^{0.5}/a(\text{H}^+)^2)$ values. In spite of the predominant role of $\text{Ca}_n\text{UO}_2(\text{CO}_3)_3^{(4-2n)-}$ complexes, the borderlines between two different species remain almost unaffected at $\text{pO}_2 \leq 55$. As observed in this exercise, the great impact of $P(\text{O}_2)$ on the aqueous speciation of U(IV)/U(VI) strongly affects its solubility under conditions relevant for nuclear waste disposal.

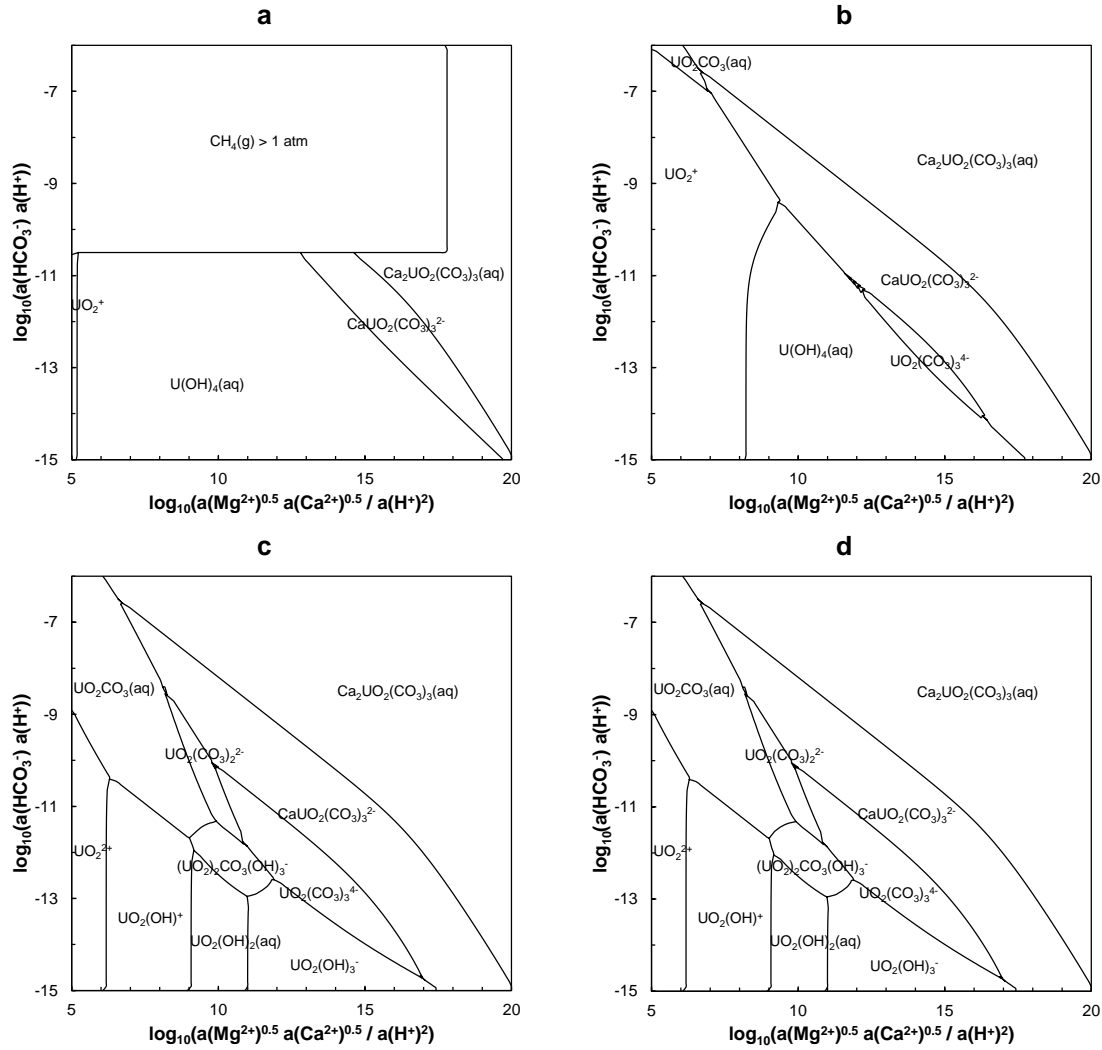


Figure 2. Activity predominance diagrams calculated using Phreeplot (Kinniburgh and Cooper, 2011) of Mg-Ca-U-OH-CO₃ calculated for $I_m = 0.1 \text{ mol kg}_w^{-1}$ NaCl using the thermodynamic data and SIT coefficients determined in Shang and Reiller (2020, 2021a). Calculations performed for $C(\text{U})_{\text{tot}} = 10^{-8} \text{ mol kg}_w^{-1}$, $P(\text{O}_2) = 10^{-73}$ (a), 10^{-67} (b), 10^{-55} (c), and 10^{-51} (d) atm.

Other activity predominance diagrams can be drawn in Figure 3 for a total uranium concentration of $10^{-6} \text{ mol kg}_w^{-1}$ at atmospheric $\text{O}_2(\text{g})$, *i.e.* $p\text{O}_2 = 0.6788$, n varying from 10^{-4} to 0.9999, and $[\text{NaCl}] = 0.5 \text{ mol kg}_w^{-1}$. The progressive transition from Ca to Mg dominated water is shown. The dominance of $\text{MgUO}_2(\text{CO}_3)_3^{2-}$ requires high ionic strength — here controlled by

NaCl — and Mg/Ca ratio — here represented by n , which are representative of seawater — see Fig. 8 in Shang and Reiller (2021a).

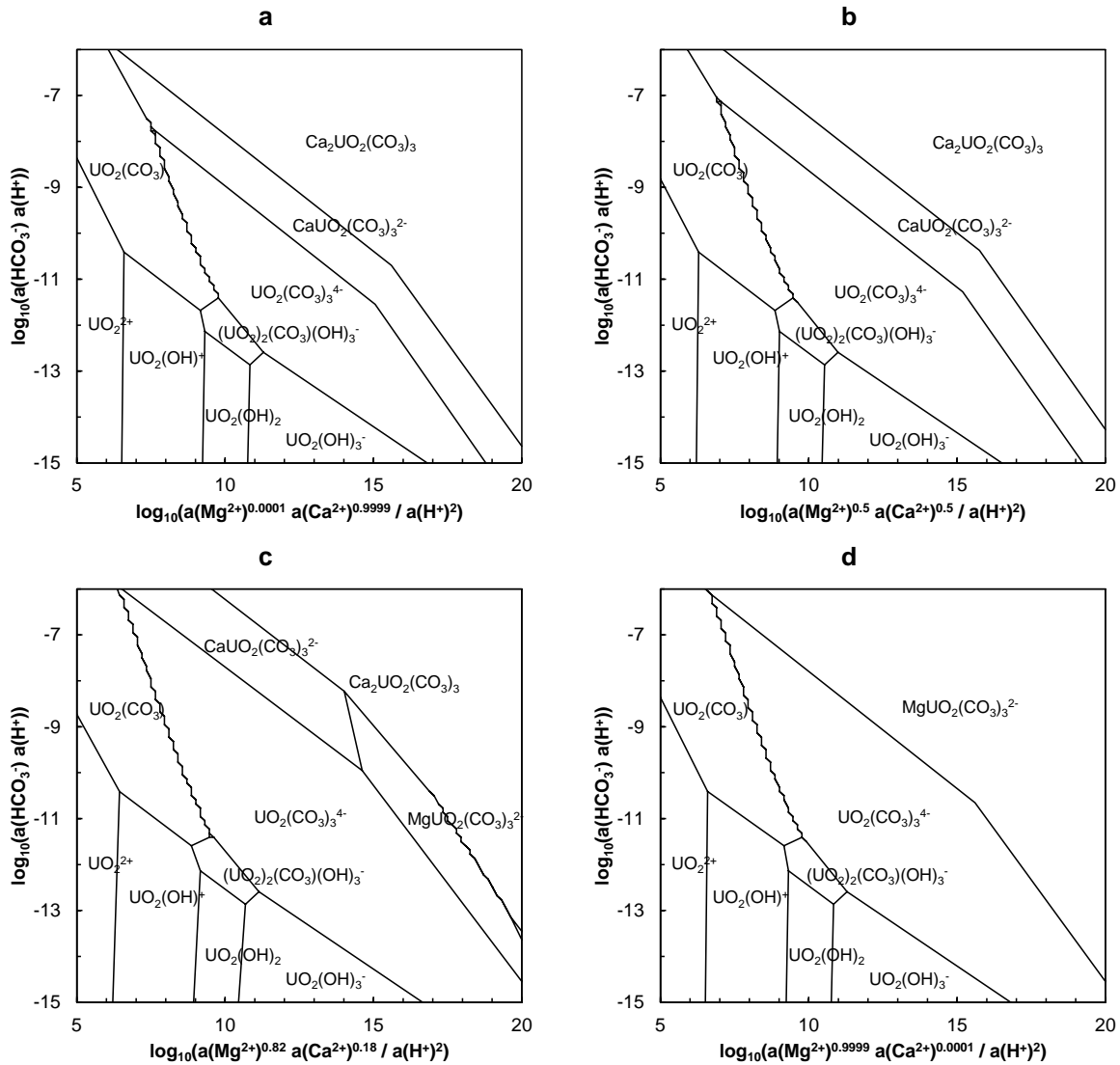


Figure 3. Activity predominance plots of 10^{-6} mol kg_w^{-1} U at $P(\text{O}_2) = 0.21$ atm and $[\text{NaCl}] = 0.5$ mol kg_w^{-1} , and varying n values

The combined influence of carbonate and NaCl concentrations are shown on the activity diagrams of Figure 4 at $n = 0.85$: the higher the value of $\log_{10}(a(\text{HCO}_3^-) a(\text{H}^+))$, the narrower the domains of $(\text{UO}_2)_n(\text{CO}_3)_l(\text{OH})_m^{2n-2l-m}$ complexes at the benefit of $\text{Ae}_n\text{UO}_2(\text{CO}_3)_3^{(4-2n)-}$; and the higher the value of $\log_{10}(a(\text{Na}^+)/a(\text{H}^+))$, the narrower the domain of $\text{Ae}_n\text{UO}_2(\text{CO}_3)_3^{(4-2n)-}$ at

the benefit of $\text{UO}_2(\text{CO}_3)_3^{4-}$. It can also be noted that the higher the $\log_{10}(a(\text{HCO}_3^-) a(\text{H}^+))$ value, the narrower the domain of $\text{MgUO}_2(\text{CO}_3)_3^{2-}$.

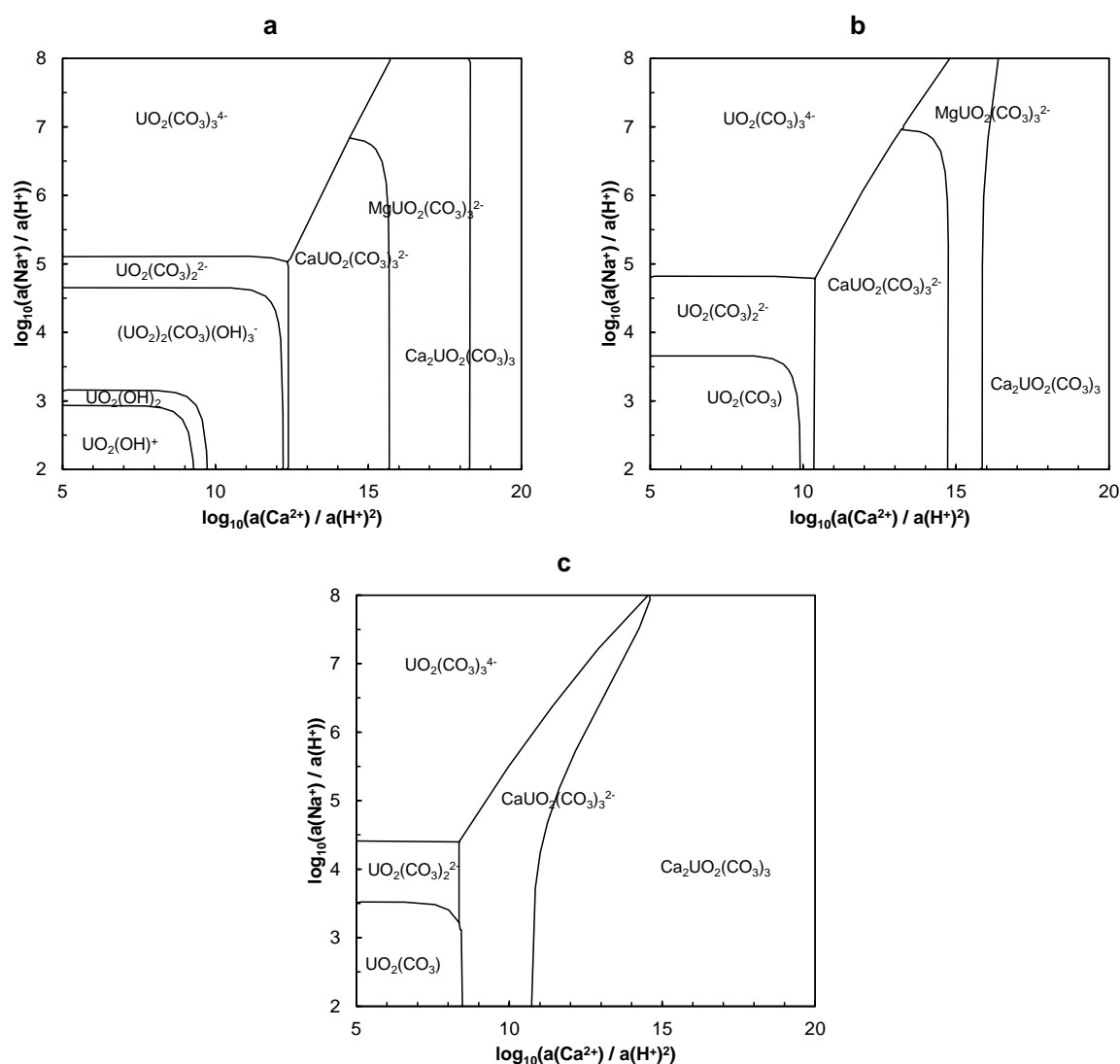


Figure 4. Activity predominance plots of $10^{-6} \text{ mol kg}_w^{-1} \text{ U}$ at $P(\text{O}_2) = 0.21 \text{ atm}$, at varying $\log_{10}(a(\text{Na}^+)/a(\text{H}^+))$ vs. $\log_{10}(a(\text{Ca}^{2+})/a(\text{H}^+)^2)$, and fixed $\log_{10}(a(\text{HCO}_3^-) a(\text{H}^+))$ values of -12 (a), -10 (b), and -8 (c).

3.3. Analysis of speciation results from water compositions

Figure S2 of the SI shows the repartition of the reported uranium concentration for the selected water compositions in this study. The measured uranium concentration varies widely from 10^{-11} to $5 \times 10^{-3} \text{ mol kg}_w^{-1}$. The ionic strength ranges from 0.6 to $83.1 \text{ mmol kg}_w^{-1}$ with an

average of $12.5 \text{ mmol kg}_w^{-1}$. Some water samples represent uranium concentration lower than $15 \text{ } \mu\text{g L}^{-1}$ ($\approx 6.30 \times 10^{-8} \text{ M}$) — the World Health Organization proposed restrictive guideline (WHO, 2017) — around the Cigar Lake mining site, Saskatchewan, Canada (Toulhoat and Beaucaire, 1993), the Oklo uranium ore deposits, from several ORANO mining sites in an ISR context (IAEA, 2001, 2016), from the European project FOREGS, and sampled in the Semipalatinsk nuclear test site (Yamamoto et al., 2010). However, concentrations $\geq 10^{-6} \text{ M}$ even up to the order of 10^{-4} M can occur in several water compositions associated with uranium ore deposits, such as in the former uranium mine at Cluff Lake, Canada (von Gunten et al., 2018), in the U ore deposits within the Lodève Basin in South Central France (Beaucaire and Toulhoat, 1987; Beaucaire et al., 2008), and in Kazakhstan (Yamamoto et al., 2010).

Some of these groundwaters containing high uranium concentration are strongly reducing, and contain important sulphide but very low calcium concentrations. The speciation distribution for the selected aqueous solutions was carried out using PHREEQC. The activity of important ions — $\log_{10} a(\text{HCO}_3^-)$, $\log_{10} a(\text{H}^+)$, $\log_{10} a(\text{Ca}^{2+})$, $\log_{10} a(\text{Na}^+)$ — and the percentages of the major species were retrieved from the output files. Saturation index of calcite and schoepite was also retrieved, which is key parameter in geochemical studies and indicates how far the solution is from thermodynamic equilibrium with respect to these minerals. In this study, we only considered the water compositions that were showing $\text{Ca}_n\text{UO}_2(\text{CO}_3)_3^{(4-2n)-}$ as major complex. The selected water compositions are plotted in $\log_{10}(a(\text{HCO}_3^-) a(\text{H}^+))$ vs. $\log_{10}(a(\text{Ca}^{2+})/a(\text{H}^+)^2)$, and $\log_{10}(a(\text{Na}^+)/a(\text{H}^+))$ vs. $\log_{10}(a(\text{Ca}^{2+})/a(\text{H}^+)^2)$ activity predominance diagrams calculated at fixed uranium concentration of $100 \text{ } \mu\text{mol kg}_w^{-1}$ and $P(\text{O}_2) = 0.2095 \text{ atm}$ at 25°C considering the activity of water to be unity. The choice of axis ranges in Figure S3 of the SI is based on the analysis of the frequency of the $\log_{10}(a(\text{Ca}^{2+})/a(\text{H}^+)^2)$ – $\log_{10}(a(\text{HCO}_3^-) a(\text{H}^+))$ – $\log_{10}(a(\text{Na}^+)/a(\text{H}^+))$ parameters. Most of selected samples within the ranges of $10 < \log_{10}(a(\text{Ca}^{2+})/a(\text{H}^+)^2) < 13$, $-11 < \log_{10}(a(\text{HCO}_3^-) a(\text{H}^+)) < -9.5$, and $4 <$

$\log_{10}(a(\text{Na}^+)/a(\text{H}^+)) < 6$. The precipitation of calcite and dolomite is not requested in calculation even if several water compositions were oversaturated respective to these phases — *cf.* Fig. S7 of ESI in Shang and Reiller (2020). The precipitation region of calcite, limited by the blue dashed line in predominance diagrams (Figure 5-Figure 9), is separately calculated by imposing the equilibrium between the atmospheric $\text{CO}_2(\text{g})$ and the aqueous solution. The mineral field boundaries of calcite were found using the “hunt and track” (*i.e.* ht1) algorithm in Phreeplot, which represents the equality of the number of moles of dissolved Ca^{2+} and precipitated CaCO_3 . The use of minstab1 calculation method, which can be adopted in constructing the mineral stability diagram, would make the borderlines move towards lower $\log_{10}(a(\text{Ca}^{2+})/a(\text{H}^+)^2)$ because it indicates the conditions where the mineral begins to precipitate. The basic principles involved in these two algorithms are detailed in Kinniburgh and Cooper (2004; 2011).

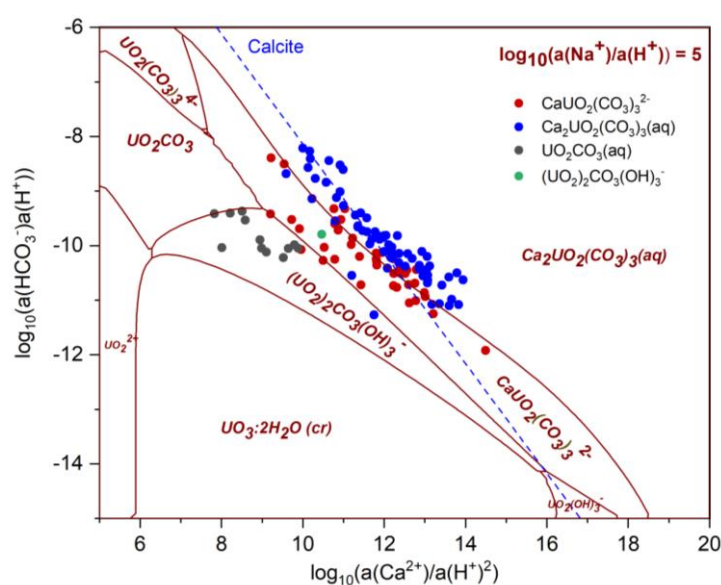


Figure 5. Predominance plot $\log_{10}(a(\text{HCO}_3^-) a(\text{H}^+))$ vs. $\log_{10}(a(\text{Ca}^{2+})/a(\text{H}^+)^2)$ at $[\text{U}(\text{VI})] = 100 \mu\text{mol kg}_w^{-1}$, $P(\text{O}_2) = 0.2095 \text{ atm}$ and fixed values of $\log_{10}(a(\text{Na}^+)/a(\text{H}^+)) = 5$. The selected sample solutions having different major species are distinguished by colour.

There are limitations in comparing all the chemical analyses of selected water compositions of different origins and types in one diagram. As shown in Figure 5, $\log_{10}(a(\text{HCO}_3^-) a(\text{H}^+))$ vs.

$\log_{10}(a(\text{Ca}^{2+})/a(\text{H}^+)^2)$ predominance diagram plotted at $\log_{10}(a(\text{Na}^+)/a(\text{H}^+)) = 5$, the positions of the points in the diagram correspond to chemistry of the studied water samples, regardless of their real values of $\log_{10}(a(\text{Na}^+)/a(\text{H}^+))$. By colour of points, the calculated major species in each water sample is presented. However, expression of natural water chemistry with the two parameters, *i.e.* $\log_{10}(a(\text{HCO}_3^-)/a(\text{H}^+))$ and $\log_{10}(a(\text{Ca}^{2+})/a(\text{H}^+)^2)$, is a drawback because the value of $\log_{10}(a(\text{Na}^+)/a(\text{H}^+))$ for a number of water samples differs from 5 units, and the borderlines of predominance regions of different complexes are closely related to this parameter. Figure 6 shows a three-dimensional repartition of the selected water samples with their values of $\log_{10}(a(\text{Na}^+)/a(\text{H}^+))$ projected to the surface parallel to the z-axis of $\log_{10}(a(\text{Na}^+)/a(\text{H}^+))$ ranging from 2 to 7. Most of the data points are plotted *ca.* $\log_{10}(a(\text{Na}^+)/a(\text{H}^+)) = 5$. A few data points are *ca.* $\log_{10}(a(\text{Na}^+)/a(\text{H}^+)) = 4$ and 6. For this reason, $\log_{10}(a(\text{HCO}_3^-)/a(\text{H}^+))$ vs. $\log_{10}(a(\text{Ca}^{2+})/a(\text{H}^+)^2)$ predominance diagrams are plotted at the three most common values of $\log_{10}(a(\text{Na}^+)/a(\text{H}^+))$, *i.e.* 4, 5, and 6.

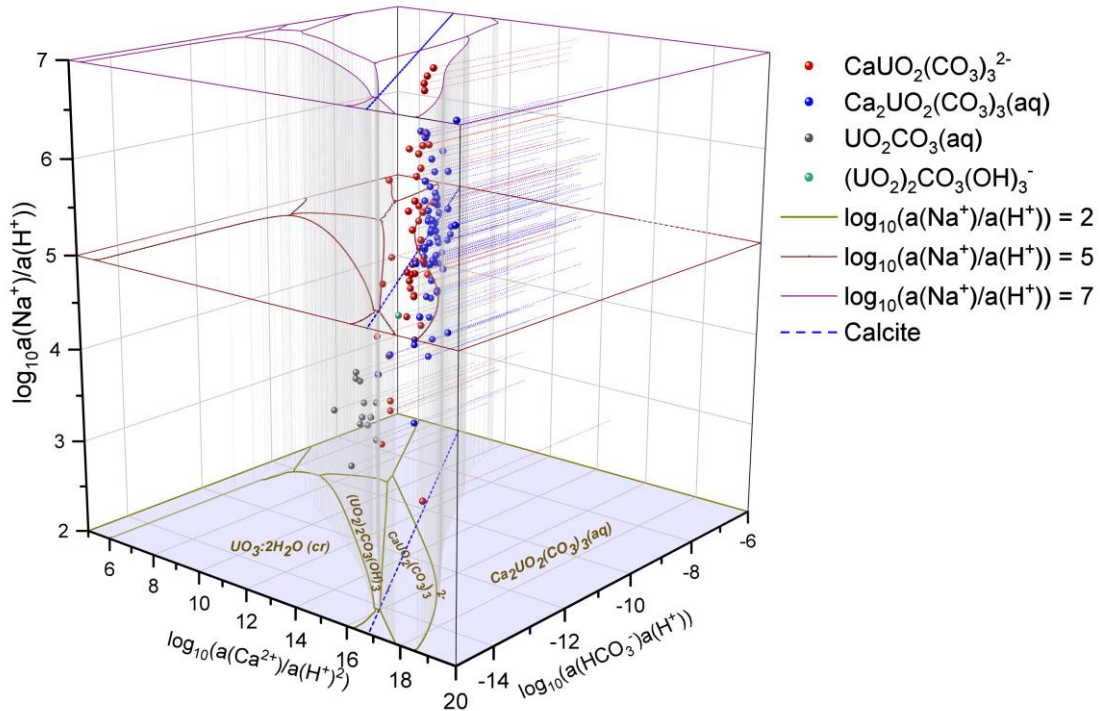


Figure 6. Repartition of the major species in the speciation calculations of the selected water compositions in a $\log_{10}(a(\text{Ca}^{2+})/a(\text{H}^+)^2)$ – $\log_{10}(a(\text{HCO}_3^-) a(\text{H}^+))$ – $\log_{10}(a(\text{Na}^+)/a(\text{H}^+))$ diagram. The values of $\log_{10}(a(\text{Na}^+)/a(\text{H}^+))$ were respectively fixed to 2, 5, and 7 to deduce the $\log_{10}(a(\text{Ca}^{2+})/a(\text{H}^+)^2)$ – $\log_{10}(a(\text{HCO}_3^-) a(\text{H}^+))$ predominance diagrams of Ca-UO₂-CO₃ system at $[\text{U}(\text{VI})] = 100 \mu\text{mol kg}_w^{-1}$, $P(\text{O}_2) = 0.21 \text{ atm}$.

The water compositions are divided into groups from their $\log_{10}(a(\text{Na}^+)/a(\text{H}^+))$ value and separately presented in the diagram having the nearest $\log_{10}(a(\text{Na}^+)/a(\text{H}^+))$ value, as shown in Figure 7. $\text{Ca}_2\text{UO}_2(\text{CO}_3)_3(\text{aq})$ can be identified in a large field at high $\log_{10}(a(\text{HCO}_3^-) a(\text{H}^+))$ and $\log_{10}(a(\text{Ca}^{2+})/a(\text{H}^+)^2)$ values in the predominance diagram with $\log_{10}(a(\text{Na}^+)/a(\text{H}^+))$ varying from 2 to 7. Actually, the variable $\log_{10}(a(\text{Na}^+)/a(\text{H}^+))$ partially reflects the ionic strength of the water samples as their pH values are comparable, and Na^+ represents one of the major cation in these water samples. It is worthy to point out that the dominant species calculated for several water samples do not strictly correspond to their position in the diagram because the predominance diagrams are calculated taking only NaCl as background electrolyte.

One can observe that the predominance regions of $\text{UO}_2(\text{CO}_3)_3^{4-}$ and $\text{CaUO}_2(\text{CO}_3)_3^{2-}$ increase with $\log_{10}(\text{a}(\text{Na}^+)/\text{a}(\text{H}^+))$ as a result of increasing interionic attraction between Ca^{2+} and other major anions. When viewed as a function of $\log_{10}(\text{a}(\text{Na}^+)/\text{a}(\text{H}^+))$ in the predominance diagram, the field of $\text{Ca}_2\text{UO}_2(\text{CO}_3)_3(\text{aq})$ constrained by the precipitation of calcite narrows with increasing $\log_{10}(\text{a}(\text{Na}^+)/\text{a}(\text{H}^+))$. Figure 7a shows that nearly all water samples in the range $3.5 < \log_{10}(\text{a}(\text{Na}^+)/\text{a}(\text{H}^+)) < 4.5$ are undersaturated with respect to calcite. Most of the selected water compositions are in the range of $4.5 < \log_{10}(\text{a}(\text{Na}^+)/\text{a}(\text{H}^+)) < 5.5$, as shown in Figure 7b. In particular, in the samples having $\text{Ca}_2\text{UO}_2(\text{CO}_3)_3(\text{aq})$ as major species calcite is oversaturated or near to the saturation line, while those dominated by $\text{CaUO}_2(\text{CO}_3)_3^{2-}$ in the aqueous phase are undersaturated, or slightly oversaturated, with respect to calcite. In the diagram where $\log_{10}(\text{a}(\text{Na}^+)/\text{a}(\text{H}^+)) = 6$, the region of $\text{Ca}_2\text{UO}_2(\text{CO}_3)_3(\text{aq})$ is completely limited by the calcite precipitation. All the samples with predominant $\text{Ca}_2\text{UO}_2(\text{CO}_3)_3(\text{aq})$ are oversaturated with respect to calcite and those with predominant $\text{CaUO}_2(\text{CO}_3)_3^{2-}$ are close to the saturation line. This observation reveals a key feature for this system, *i.e.* the $\text{Ca}_2\text{UO}_2(\text{CO}_3)_3(\text{aq})$ complex is controlling the U(VI) speciation in the aqueous phase saturated with calcite depending on the value of $\log_{10}(\text{a}(\text{Na}^+)/\text{a}(\text{H}^+))$, or approximately on the ionic strength. It is worth noting that the samples with $\text{UO}_2\text{CO}_3(\text{aq})$ as major species are filtered out in these predominance diagrams as their values $2.08 \leq \log_{10}(\text{a}(\text{Na}^+)/\text{a}(\text{H}^+)) \leq 3.38$ are too low to be represented in these projections.

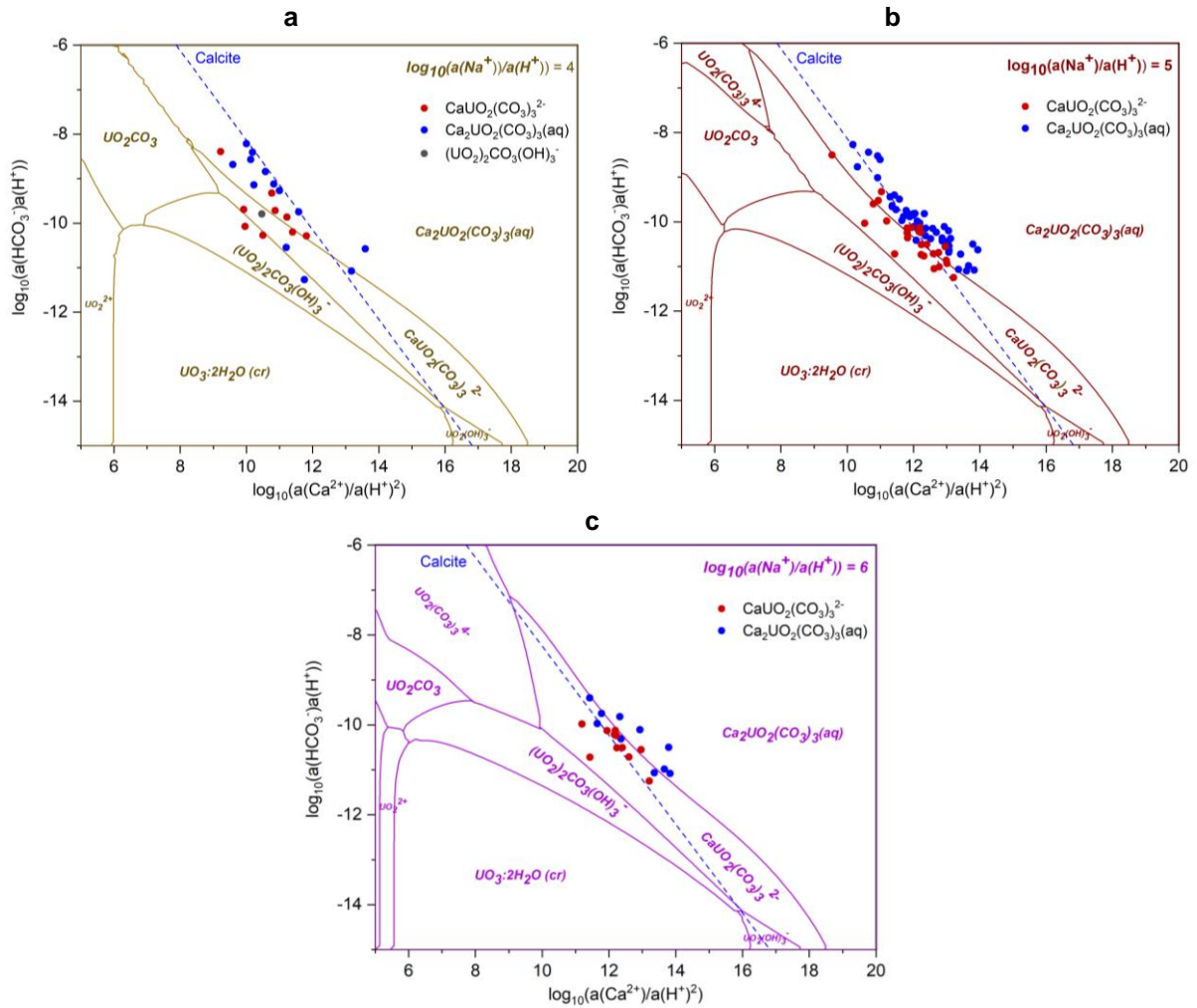


Figure 7. Major uranium species obtained in the speciation calculations of the selected water compositions of which (a) $3.5 < \log_{10}(a(\text{Na}^+)/a(\text{H}^+)) < 4.5$, (b) $4.5 < \log_{10}(a(\text{Na}^+)/a(\text{H}^+)) < 5.5$, and (c) $5.5 < \log_{10}(a(\text{Na}^+)/a(\text{H}^+)) < 6.5$.

Figure S4 of the SI focuses on the repartition of the selected water samples in a $\log_{10}(a(\text{Ca}^{2+})/a(\text{H}^+)^2) - \log_{10}(a(\text{Na}^+)/a(\text{H}^+)) - \log_{10}(a(\text{HCO}_3^-)a(\text{H}^+))$ diagram with the z-axis varying from -12 to -8. Most of the data points are in the range of $-11 < \log_{10}(a(\text{HCO}_3^-)a(\text{H}^+)) < -9$.

The diagrams of $\log_{10}(a(\text{Ca}^{2+})/a(\text{H}^+)^2)$ vs. $\log_{10}(a(\text{Na}^+)/a(\text{H}^+))$ with $\log_{10}(a(\text{HCO}_3^-)a(\text{H}^+)) = -11, -10.5, -10$ and -9.5 were chosen for the representation in Figure 8. The data points were categorized from their values of $\log_{10}(a(\text{HCO}_3^-)a(\text{H}^+))$ and presented in the diagram having the

nearest value of $\log_{10}(a(\text{HCO}_3^-) a(\text{H}^+))$. The water sample symbols are contoured by black squares when calcite is undersaturated in solution under their individual and specific conditions, and by red squares when the calcite is oversaturated in solution. Again, the saturation state with respect to calcite and the dominant species in several water samples during the calculation do not correspond to their position in the diagram because the predominance diagrams are constructed taking only NaCl as background electrolyte. Nonetheless, these particular samples are all near to the borderlines. Figure 8 again highlights the importance of calcite saturation in this system. At $\log_{10}(a(\text{HCO}_3^-) a(\text{H}^+)) = -11$, the solution would easily be oversaturated with respect to calcite while high values of $\log_{10}(a(\text{HCO}_3^-) a(\text{H}^+))$ promote the predominance of uranyl-carbonate complexes. The predominance of the binary/ternary complexes $\text{UO}_2\text{CO}_3/\text{CaUO}_2(\text{CO}_3)_3^{2-}/\text{Ca}_2\text{UO}_2(\text{CO}_3)_3(\text{aq})$ depends on the activity of calcium owing to the close pH values in the selected water samples. High concentration of calcium in system leads to the precipitation of calcite before having the $\text{Ca}_2\text{UO}_2(\text{CO}_3)_3(\text{aq})$ as major species in the aqueous phase.

The selected water solutions are colored according to their predominant species in Figure 8. For each group, an ellipsoid containing most of the data points belonging to that group is constructed using Hotelling's T-squared (T^2) distribution. (<https://www.originlab.com/fileExchange/details.aspx?fid=280>), as shown in Figure 9. Equations of the ellipsoids are reported in Table 1. For this reason, the ellipsoidal boundaries of $\text{UO}_2\text{CO}_3(\text{aq})$, $\text{CaUO}_2(\text{CO}_3)_3^{2-}$, and $\text{Ca}_2\text{UO}_2(\text{CO}_3)_3(\text{aq})$ were determined from the distribution of sample points in $\log_{10}(a(\text{Ca}^{2+})/a(\text{H}^+)^2) - \log_{10}(a(\text{Na}^+)/a(\text{H}^+)) - \log_{10}(a(\text{HCO}_3^-) a(\text{H}^+))$ diagram with the interval confidence of 68%, corresponding to 1σ . Using a higher confidence level, *i.e.* 95% or 98%, would generate wider ellipsoids, which tend to produce a larger intersection between the two ellipsoids of $\text{CaUO}_2(\text{CO}_3)_3^{2-}$ and $\text{Ca}_2\text{UO}_2(\text{CO}_3)_3(\text{aq})$, thus a less clear distinction of their concentration domain.

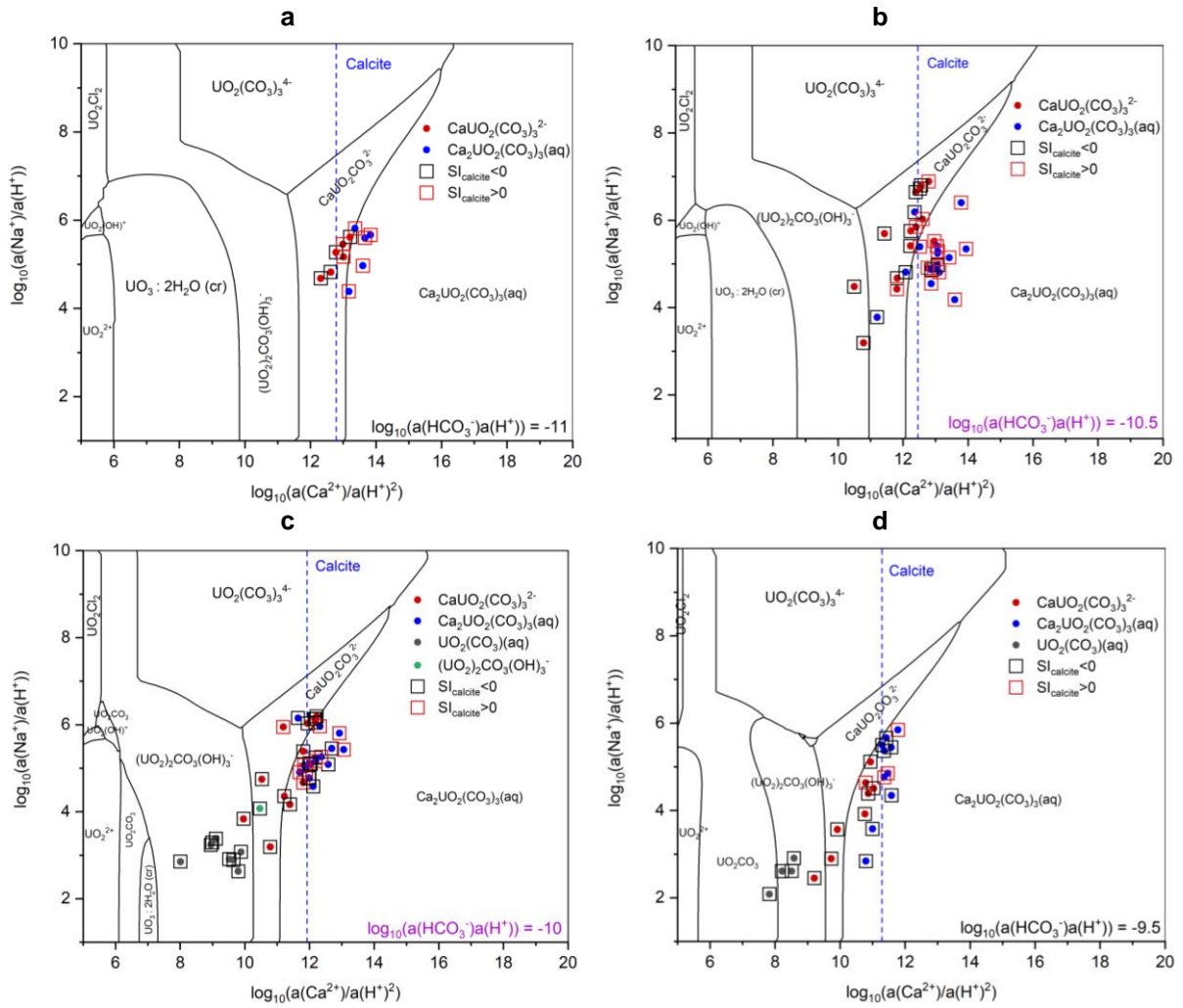


Figure 8. Major uranium species obtained in the speciation calculations of the selected water compositions in ranges of: (a) $-11.5 < \log_{10}(a(\text{HCO}_3^-) a(\text{H}^+)) < -10.5$; (b) $-11 < \log_{10}(a(\text{HCO}_3^-) a(\text{H}^+)) < -10$; (c) $-10.5 < \log_{10}(a(\text{HCO}_3^-) a(\text{H}^+)) < -9.5$; and (d) $-10 < \log_{10}(a(\text{HCO}_3^-) a(\text{H}^+)) < -9$.

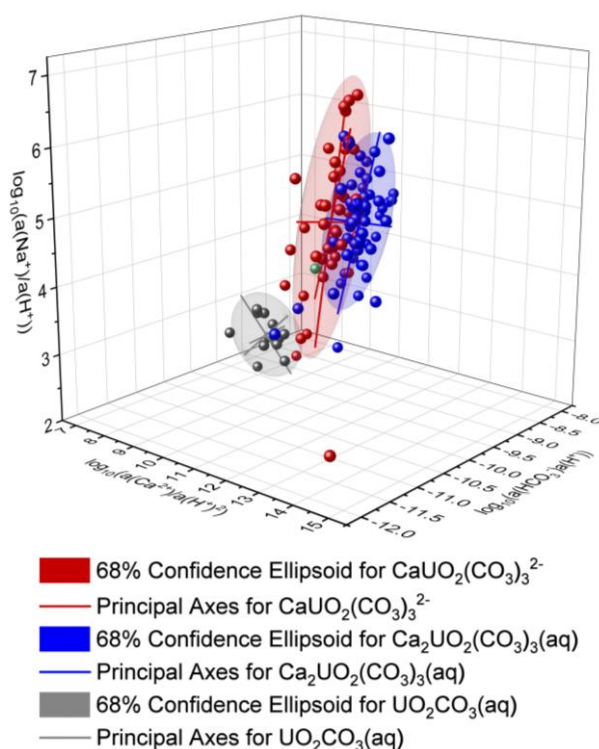


Figure 9. Ellipsoidal predominance regions of $\text{UO}_2\text{CO}_3(\text{aq})$ (grey), $\text{CaUO}_2(\text{CO}_3)_3^{2-}$ (red), and $\text{Ca}_2\text{UO}_2(\text{CO}_3)_3(\text{aq})$ (blue) in $\log_{10}(a(\text{Ca}^{2+})/a(\text{H}^+)^2) - \log_{10}(a(\text{Na}^+)/a(\text{H}^+)) - \log_{10}(a(\text{HCO}_3^-)/a(\text{H}^+))$ space determined from the sample point-clouds with the interval confidence of 68%.

To allow representation, Figure 9, and Figure S5 from the SI, illustrates the confidence ellipsoids for three species using 2D projections seen in different view angles. One can note that the ellipsoid of $\text{Ca}_2\text{UO}_2(\text{CO}_3)_3(\text{aq})$ is slightly narrower and more elongated than that of $\text{CaUO}_2(\text{CO}_3)_3^{2-}$. The overlap of the calculated ellipsoids of $\text{CaUO}_2(\text{CO}_3)_3^{2-}$, and $\text{Ca}_2\text{UO}_2(\text{CO}_3)_3(\text{aq})$ can nearly extend to the half of their individual volumes. Furthermore, the ellipsoid of $\text{Ca}_2\text{UO}_2(\text{CO}_3)_3(\text{aq})$ is located in the regions of higher calcium and carbonate concentrations compared with that of $\text{CaUO}_2(\text{CO}_3)_3^{2-}$, which is consistent with the evaluation of equilibrium constants. Regarding to the concentration region of $\text{UO}_2\text{CO}_3(\text{aq})$, its ellipsoid exists at low $\log_{10}(a(\text{Na}^+)/a(\text{H}^+))$ and low $\log_{10}(a(\text{Ca}^{2+})/a(\text{H}^+)^2)$, underlining that the occurrence of major $\text{UO}_2\text{CO}_3(\text{aq})$ in aqueous phase is due to a low calcium concentration in solution.

Nevertheless, it is noteworthy that the pH value is also an important parameter as the samples with $\text{UO}_2\text{CO}_3(\text{aq})$ as major species are all mildly acidic of pH value between 6 and 7, which is less favorable to the formation of $\text{CaUO}_2(\text{CO}_3)_3^{2-}$, and $\text{Ca}_2\text{UO}_2(\text{CO}_3)_3(\text{aq})$ especially at low calcium concentration, contrary to water from Lodève in Beaucaire and Toulhoat (1987).

The authors noticed the particular importance of Mg^{2+} in the selected water solutions. Figure S6 of the SI shows the ellipsoids determined from the distribution of samples points in $\log_{10}((a(\text{Mg}^{2+})^n a(\text{Ca}^{2+})^{(1-n)}/a(\text{H}^+)^2) - \log_{10}(a(\text{Na}^+)/a(\text{H}^+)) - \log_{10}(a(\text{HCO}_3^-) a(\text{H}^+)))$ diagram, where the ratio $n = a(\text{Mg}^{2+})/(a(\text{Mg}^{2+}) + a(\text{Ca}^{2+}))$ is calculated illustrating the importance of $\text{MgUO}_2(\text{CO}_3)_3^{2-}$. Equations of the ellipsoids are accordingly reported in Table S2 of the SI. The shift of sample points along the x-axis as well as the resulting ellipsoidal patterns do not show large differences. However, it is rather remarkable that the use of ratio n could better predict the predominant species for the water compositions of important $\log_{10}a(\text{Mg}^{2+})$ — see the comparison for the site du Bosc samples in the next section.

Table 1. Equations of the principal axes of the ellipsoids for $\text{CaUO}_2(\text{CO}_3)_3^{2-}$, $\text{Ca}_2\text{UO}_2(\text{CO}_3)_3(\text{aq})$, and $\text{UO}_2\text{CO}_3(\text{aq})$ species.

	Principal semi-axes	First Principal Axis	Second Principal Axis	Third Principal Axis
$\text{CaUO}_2(\text{CO}_3)_3^{2-}$	a = 2.92826 b = 1.73083 c = 0.50823	x = 11.6672 – 0.755377 t y = -10.2206 + 0.352514 t z = 4.99219 – 0.552395 t	x = 11.6672 + 0.41258 t y = -10.2206 – 0.399069 t z = 4.99219 – 0.818854 t	x = 11.6672 – 0.509101 t y = -10.2205 – 0.84645 t z = 4.99219 + 0.156008 t
$\text{Ca}_2\text{UO}_2(\text{CO}_3)_3(\text{aq})$	a = 2.66282 b = 1.21166 c = 0.518076	x = 11.9882 – 0.793119 t y = -9.89187 + 0.521319 t z = 4.94291 – 0.314943 t	x = 11.9882 – 0.119187 t y = -9.89187 + 0.37425 t z = 4.94291 – 0.919636 t	x = 11.9882 + 0.59729 t y = -9.89187 + 0.766918 t z = 4.94291 – 0.23469 t
$\text{UO}_2\text{CO}_3(\text{aq})$	a = 1.77066 b = 0.752217 c = 0.41014	x = 8.92073 – 0.900444 t y = -9.84455 + 0.32475 t z = 2.87246 – 0.289368 t	x = 8.92073 – 0.402997 t y = -9.84455 – 0.372517 t z = 2.87246 + 0.835957 t	x = 8.92073 + 0.163688 t y = -9.84455 + 0.869347 t z = 2.87246 + 0.466306 t

3.4. Comparison of modelling and experimental results for the water samples collected from the site du Bosc

3.4.1. Water from the site du Bosc

Table 2 lists the chemical constituents for the investigated water samples: one was the untreated water initially at pH 8.3, and the other one was initially treatment by acidification to pH 6.5 after sampling. It is apparent that the acidification of the solution did not last until it was analyzed and the buffer capacity of the waters — most likely through the dissolution of calcium carbonate — imposes a final pH 8.16, close to the untreated one. In the second sample, the increase of SO_4^{2-} reflected the added amount of H_2SO_4 . It is also worthy to notice that the Ca content in the second sub sample was increased *ca.* three fold compared to the first sub sample, when there was no difference between the Mg contents. This could suggest that a Ca containing phase was dissolved during the acidification process. The slight (and barely significant) increase in alkalinity maybe an indication of the dissolution of, most likely, calcite particles. The TOC content appears relatively low, as in Drozdak et al. (2016a), but significant and comparable in the both samples. Even if the complexation of U(VI) by natural organic matter is known since long — Reiller (2010, 2015), Reiller et al. (2012) and references therein —, it will not be taken into account in a first approach. The differences between the water composition in Drozdak et al. (2016a) and the ones analyzed here is representative of the variability of the treated waters from the site du Bosc.

Table 2. Chemical constituents for the investigated site du Bosc water samples.

	untreated water	treated water
pH	8.30	8.16
F ⁻ (mmol L ⁻¹)	< lod*	< lod*
Cl ⁻ (mmol L ⁻¹)	0.66 ± 0.05	0.65 ± 0.05
SO ₄ ²⁻ (mmol L ⁻¹)	5.51 ± 0.39	6.84 ± 0.48
Alkalinity (mmol L ⁻¹)	4.51 ± 0.32	5.16 ± 0.36
Na ⁺ (mmol L ⁻¹)	8.17 ± 0.57	8.00 ± 0.56
K ⁺ (mmol L ⁻¹)	0.49 ± 0.03	0.50 ± 0.04
Mg ²⁺ (mmol L ⁻¹)	2.74 ± 0.19	2.82 ± 0.20
Ca ²⁺ (mmol L ⁻¹)	0.78 ± 0.05	2.54 ± 0.18
TOC ppmc	4.2 ± 1.2	3.7 ± 1.3
U (μmol L ⁻¹)	70.5 ± 12.3	n.m.
I _m (mmol kg _w ⁻¹)	21.8	26.9

* lod: limit of detection = 10⁻⁵ mol_F L⁻¹; n.m. not measured; values expressed ± 1σ

3.4.2. Modelling of inorganic speciation

With the detailed chemical compositions for the untreated and treated waters sampled from the site du Bosc (Table 2, and Figure S8a of the SI), their uranium speciation calculations were performed using $\log_{10}\beta^\circ$, $\Delta_f H_m^\circ$, and SIT parameters $\varepsilon((\text{Mg}/\text{Ca})_n\text{UO}_2(\text{CO}_3)_3^{(4-2n)-}, \text{Na}^+\text{Cl}^-)$ from Shang and Reiller (2020, 2021a, b) implemented in the input file for PHREEQC and using Thermochemie 10a database — the oversaturation of CaCO₃ and MgCa(CO₃)₂ phases are shown in Figure S8b of the SI. The comparison with the discharge water from the site du Bosc in Drozdak et al. (2016a) is also presented. The percentages of major uranium carbonate species, the activity of important ions, as well as the values of $\log_{10}(a(\text{Ca}^{2+})/a(\text{H}^+)^2)$, $\log_{10}(a(\text{Na}^+)/a(\text{H}^+))$, and $\log_{10}(a(\text{HCO}_3^-) a(\text{H}^+))$ are listed in Table 3 — one can see that using either SIT or Davies equation does not change the results significantly. The ratio $n = a(\text{Mg}^{2+})/(a(\text{Mg}^{2+}) + a(\text{Ca}^{2+}))$ is calculated illustrating the importance of MgUO₂(CO₃)₃²⁻. The increase of Ca in the treated water is reflected in the decrease of the n value and of the percentage of MgUO₂(CO₃)₃²⁻ (Table 3).

As displayed in Figure 10, the position of the investigated samples are well included in the previously determined ellipsoids for CaUO₂(CO₃)₃²⁻ (red) and Ca₂UO₂(CO₃)₃(aq) (blue). As with the untreated water sample, the red point is actually located in the overlap between

ellipsoids of $\text{CaUO}_2(\text{CO}_3)_3^{2-}$ and $\text{Ca}_2\text{UO}_2(\text{CO}_3)_3(\text{aq})$, indicating that the dominant species cannot be unambiguously assigned without thermodynamic calculation in the $\log_{10}(a(\text{Ca}^{2+})/a(\text{H}^+)^2) - \log_{10}(a(\text{Na}^+)/a(\text{H}^+)) - \log_{10}(a(\text{HCO}_3^-) a(\text{H}^+))$ diagram. However, this red point is well positioned in the $\text{CaUO}_2(\text{CO}_3)_3^{2-}$ ellipsoidal predominance region in $\log_{10}((a(\text{Mg}^{2+})^n a(\text{Ca}^{2+})^{(1-n)})/a(\text{H}^+)^2) - \log_{10}(a(\text{Na}^+)/a(\text{H}^+)) - \log_{10}(a(\text{HCO}_3^-) a(\text{H}^+))$ space (see Figure S7 of the SI). According to the thermodynamic modelling, $\text{CaUO}_2(\text{CO}_3)_3^{2-}$ is expected to be the most abundant species in untreated water with percentage of 50.6% and the sum of -2 charge bearing ternary complexes ($\text{CaUO}_2(\text{CO}_3)_3^{2-}$ and $\text{MgUO}_2(\text{CO}_3)_3^{2-}$) attains 76.7% (Table 3).

One can observe that the blue point representing the treated water is solely included in the ellipsoids of $\text{Ca}_2\text{UO}_2(\text{CO}_3)_3(\text{aq})$ in $\log_{10}(a(\text{Ca}^{2+})/a(\text{H}^+)^2)$ -axis diagram (Figure 10), suggesting a predominance of $\text{Ca}_2\text{UO}_2(\text{CO}_3)_3(\text{aq})$ in aqueous solution. The verification of dominant complex for the treated sample corroborates also the results of the speciation calculation as the percentage of the principal species — $\text{Ca}_2\text{UO}_2(\text{CO}_3)_3(\text{aq})$ is of 50.8% (Table 3).

One can conclude that the determination of ellipsoids for $\text{Ca}_n\text{UO}_2(\text{CO}_3)_3^{(4-2n)-}$ complexes is a suitable tool for quickly identifying the major (calcium) uranyl carbonate species for a given natural water sample once its chemical composition is available. As stressed out by Reiller and Descostes (2020), comparable results could be obtained with the later version of PRODATA database file (Reiller, 2022), containing data from Shang and Reiller (2020, 2021a, b), now used for environmental monitoring of ORANO Mining activities (Besançon et al., 2020; Grozeva et al., 2022; Lartigue et al., 2020; Seigneur et al., 2021).

In a later stage, the calculation results will be compared with the uranium speciation identified by the TRLFS analyses.

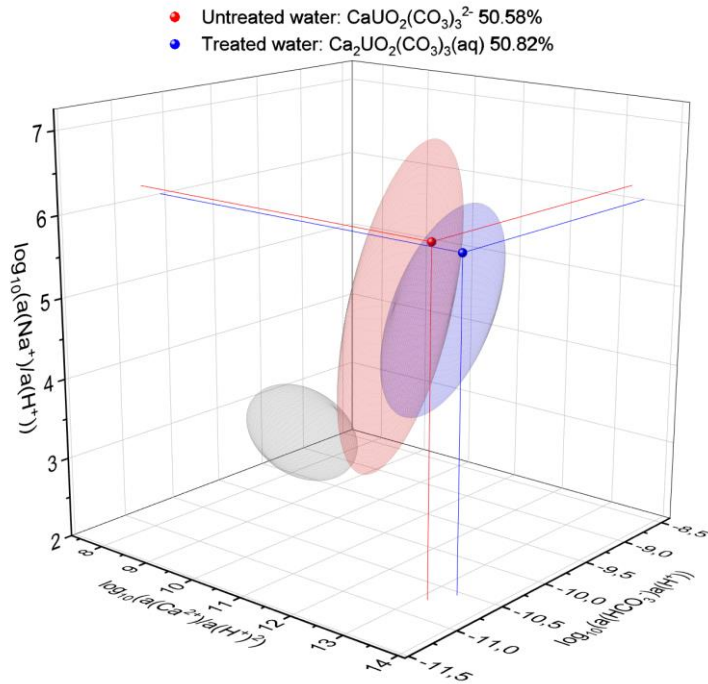


Figure 10. Position of the two waters from the site du Bosc in a $\log_{10}(a(\text{Ca}^{2+})/a(\text{H}^+)^2)$ – $\log_{10}(a(\text{Na}^+)/a(\text{H}^+))$ – $\log_{10}(a(\text{HCO}_3^-)/a(\text{H}^+))$ diagram. Ellipsoidal predominance regions of $\text{UO}_2\text{CO}_3(\text{aq})$ (grey), $\text{CaUO}_2(\text{CO}_3)_3^{2-}$ (red), and $\text{Ca}_2\text{UO}_2(\text{CO}_3)_3(\text{aq})$ (blue) space determined from the sample point-clouds with the interval confidence of 68% (Figure 9).

Table 3. Percentages of major uranium carbonate species — see Figure S8a of the SI for a graphical representation — and logarithm of major ions activities calculated using Thermochimie 10a database file (Giffaut et al., 2014; Grivé et al., 2015) for the site du Bosc.

Samples	Discharge ^a	untreated water		treated water	
		SIT	SIT	Davies	SIT
CaUO ₂ (CO ₃) ₃ ²⁻	44.5%	50.1%	50.2%	43.0%	43.3%
MgUO ₂ (CO ₃) ₃ ²⁻	6.4%	27.7%	27.8%	7.1%	7.2%
Ca ₂ UO ₂ (CO ₃) ₃ (aq)	47.6	18.4%	18.2%	48.7%	48.3%
UO ₂ (CO ₃) ₃ ⁴⁻	1.2%	3.6%	3.7%	1.1%	1.1%
Total	99.7%	99.9%	99.9%	99.9%	100.0%
log ₁₀ P(CO ₂ (g))	-1.78	-2.96	-2.96	-2.75	-2.75
log ₁₀ a(Ca ²⁺)	-2.99	-3.48	-3.48	-2.97	-2.97
log ₁₀ a(Mg ²⁺)	-3.04	-2.93	-2.94	-2.95	-2.95
log ₁₀ a(HCO ₃ ⁻)	-2.25	-2.48	-2.48	-2.41	-2.41
log ₁₀ a(Na ⁺)	-2.07*	-2.15	-2.15	-2.16	-2.16
log ₁₀ a(H ⁺)	-7.35	-8.30	-8.30	-8.16	-8.16
log ₁₀ (a(Ca ²⁺)/a(H ⁺) ²)	11.71	13.12	13.12	13.35	13.35
log ₁₀ (a(Mg ²⁺)/a(H ⁺) ²)	11.66	13.67	13.66	13.37	13.37
n = a(Mg ²⁺)/(a(Mg ²⁺)+a(Ca ²⁺))	0.47	0.78	0.78	0.51	0.51
log ₁₀ (a(Mg ²⁺) ⁿ a(Ca ²⁺) ¹⁻ⁿ /a(H ⁺) ²)	11.69	13.55	13.54	13.36	13.36
log ₁₀ (a(HCO ₃ ⁻) a(H ⁺))	-9.60	-10.78	-10.78	-10.57	-10.57
log ₁₀ (a(Na ⁺)/a(H ⁺))	5.28	6.15	6.15	6.00	6.00
I _m (mol kg _w ⁻¹)	0.027	0.022	0.022	0.027	0.027

^a Drozdak et al. (2016a)

* calculated from electrical balance.

3.4.3. Spectroscopic measurement

TRLFS can help elucidating the speciation of uranium in water because of the very low detection limits, a high sensitivity with respect to U(VI) complex, and its triple selectivity — *i.e.*, selectivity in excitation wavelength, emission spectrum, and time-resolved acquisition. In general, TRLFS provides two important spectroscopic pieces of information: characteristic luminescence decay time and positions of the emission maxima. In a fingerprinting procedure, the recorded TRLFS spectra can be identified with the help of previously acquired reference complexes. In the previously published works (Shang and Reiller, 2020; Shang et al., 2020; Shang and Reiller, 2021a, b), we have obtained these primary spectroscopic information for (Mg/Ca)_nUO₂(CO₃)₃⁽⁴⁻²ⁿ⁾⁻ complexes under varying conditions — type of electrolyte, ionic

strength and temperature — that will be compared with the recorded spectra of the site du Bosc water samples.

The two natural occurring water samples in the Site du Bosc both delivered a measurable luminescence signal, which is characteristic for uranyl carbonate luminescence. Figure 11a shows the emission spectra normalized to their total area for each sample with initial delay time of $D = 25$ ns during the gate width $W = 1$ μ s, in comparison with a reference solution of known composition in which U(VI) principally exists in the form of $\text{Ca}_n\text{UO}_2(\text{CO}_3)_3^{(4-2n)-}$ complexes. Hypsochromic-shifted peak positions compared with those of UO_2^{2+} ions (470.07, 487.31, 509.31, 533.38, and 559.86 nm) in acidic conditions provide evidence for formation of triscarbonatouranyl(VI) complexes in aqueous solution. The characteristic peak positions are the same with the reference solution. Nevertheless, the water from the sample site represents an obvious distortion in the spectrum. This distortion does not seem to be identical for the two water samples: the acidification to pH *ca.* 6.5 seems to have a slight influence on the initial spectrum. An acquisition of the same solutions was also made at a longer delay time ($D = 100$ ns), in order to verify whether the distortion is due to the luminescence of another U(VI) complex having a different decay time. As illustrated in Figure 11b, the luminescence spectra of the two water samples with $D = 100$ ns are identical to that of $\text{Ca}_n\text{UO}_2(\text{CO}_3)_3^{(4-2n)-}$ complexes. It is therefore possible to hypothesize that two decay functions of U(VI) are involved in the water samples: a fast decay function not yet identifiable, and a slower decay function of which the spectrum is characteristic of $\text{Ca}_n\text{UO}_2(\text{CO}_3)_3^{(4-2n)-}$ complexes.

It is noteworthy that the contribution of the $\text{MgUO}_2(\text{CO}_3)_3^{2-}$ complex to the general luminescence in the untreated water sample — which account of *ca.* 26% of the total uranium speciation —, is not easy to settle, as the luminescence spectra of $(\text{Mg}/\text{Ca})_n\text{UO}_2(\text{CO}_3)_3^{(4-2n)-}$ complexes are difficult to distinguish (Oher et al., 2020; Shang and

Reiller, 2021a). Moreover, relatively low amount of $\text{MgUO}_2(\text{CO}_3)_3^{2-}$ would impede its identification using a $300 \text{ lines mm}^{-1}$ grating.

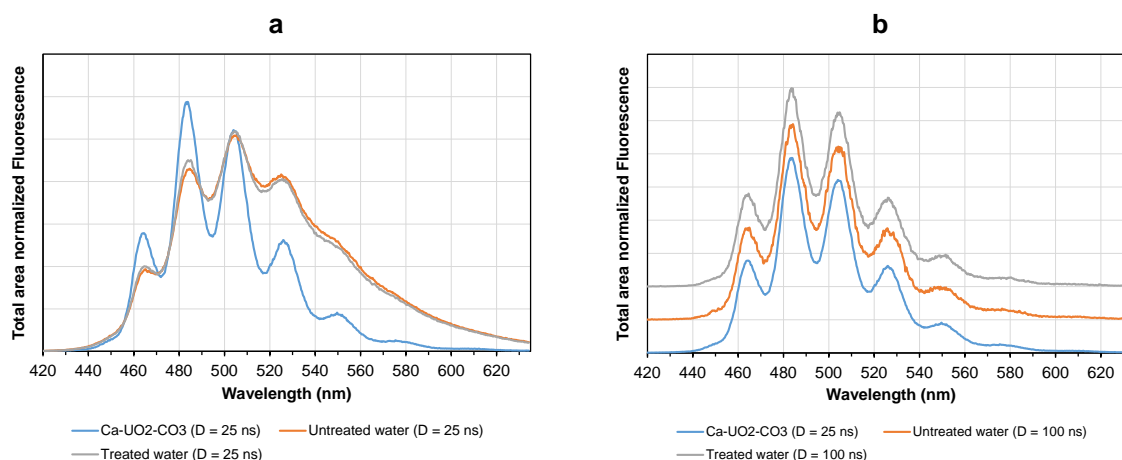


Figure 11. Comparison of luminescence spectra normalized to the same area of uranium in a reference solution (blue), in the untreated water sample (orange) and in the treated water (grey) from the site du Bosc (LOD): (a) initial delay time of $D = 25 \text{ ns}$ and gate width $W = 1 \mu\text{s}$; (b) initial delay time of $D = 100 \text{ ns}$ and gate width $W = 1 \mu\text{s}$, baselines are shifted for better visualization.

The luminescence decay of the untreated water sample was acquired by recording the luminescence spectra as a function of delay time. Figure S9a of the SI shows the spectra normalized to the same area for the delay time ranging from 20 to 215 ns in steps of 5 ns with gate width $W = 50 \text{ ns}$, which is more favorable to distinguish the spectra of different species. Figure S9b of the SI shows the exponential fits of integrated time-resolved luminescence intensities in the wavelength range from 420 to 635 nm using the trapezoid method. A mono-exponential luminescence decay (dashed curve in Figure S9b of the SI) is clearly not satisfactory to describe the decay process with $\tau = (31 \pm 1) \text{ ns}$, while a bi-exponential function can better fit the luminescence decay curves with $\tau_1 = (11 \pm 1) \text{ ns}$ (dotted curve) and $\tau_2 = (38 \pm 1) \text{ ns}$ (dash-dot curve).

The bi-exponential decay of the TRLFS-signals for the untreated water sample revealed that either two luminescent fluorophores were observed, or the rate of de-excitation process is slower than that of ligand exchange. However, for such complicated fluorophores, luminescence decay behaviour cannot be simply settled. With the determined parameters in bi-exponential function, it is possible to estimate the spectral contributions of the individual species, *e.g.*, the second component contributes 29% at $D = 20$ ns, and 98% at $D = 100$ ns and the first component represents 71% of the luminescent signal at $D = 20$ ns. This allows the spectral decomposition of the experimental spectrum at $D = 20$ ns, as shown in Figure 12.

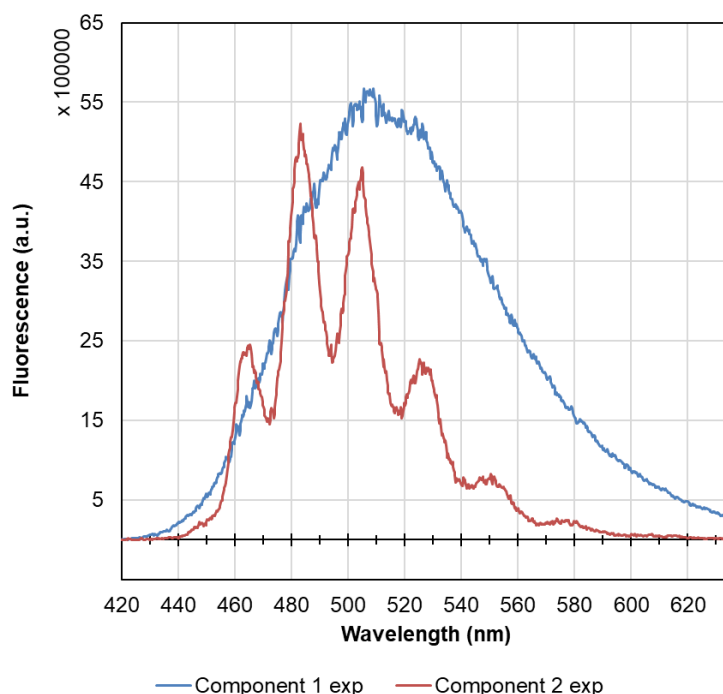


Figure 12. Decomposition of uranium luminescence signal as a function of delay time in acquisition for the untreated water from the site du Bosc.

In experiments, we observed that the luminescence spectra for the same water sample under identical measurement conditions have undergone evident spectral modification after long time laser excitation, as shown in Figure S10 of the SI. It is well known that the dissolved organic matter present in natural waters can impair the detection of total uranium because of the complexation of organic species, such as humic substances, with uranyl ion (Czerwinski et al.,

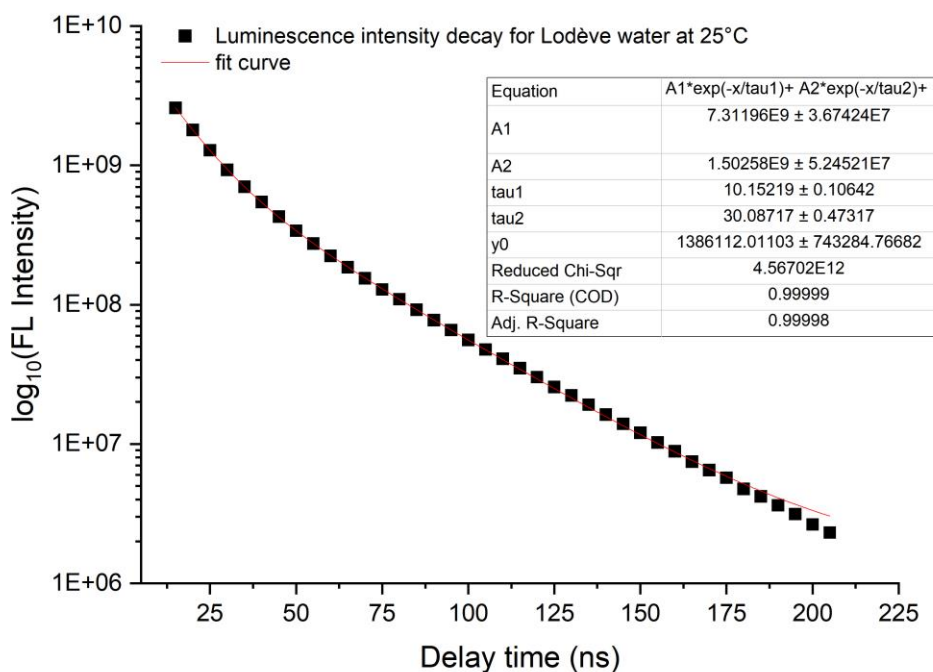
1994; Sachs et al., 2007; Steudtner et al., 2011a). One can expect luminescence emission of these ligands if they contain delocalized p-electron system, like in aromatic compounds (Geipel et al., 2004; Sachs et al., 2007). The previous determination of decay times using bi-exponential fits (Figure S9 of the SI) suggests the existence of organic moieties in the aqueous system due to the very short decay time of $\tau_1 = (11 \pm 1)$ ns. Steudtner et al. (2011a; 2011b) suggested that a mixed complex containing $\text{UO}_2\text{-CO}_3$ -humic acid was formed under carbonated conditions.

A set of luminescence decays was recorded for the long time-excited site du Bosc water sample at 25°C. As shown in the fitting results in the Figure 13, the luminescence decays bi-exponentially within the delay range studied. The equation: $\text{Intensity} = A_1\exp(-x/\tau_1) + A_2\exp(-x/\tau_2) + y_0$ was applied in the fitting procedure where A_1 , A_2 represent the luminescence intensity of components 1 and 2 at $D = 0$, τ_1 and τ_2 correspond to their decay times and y_0 is an adjustable noise term.

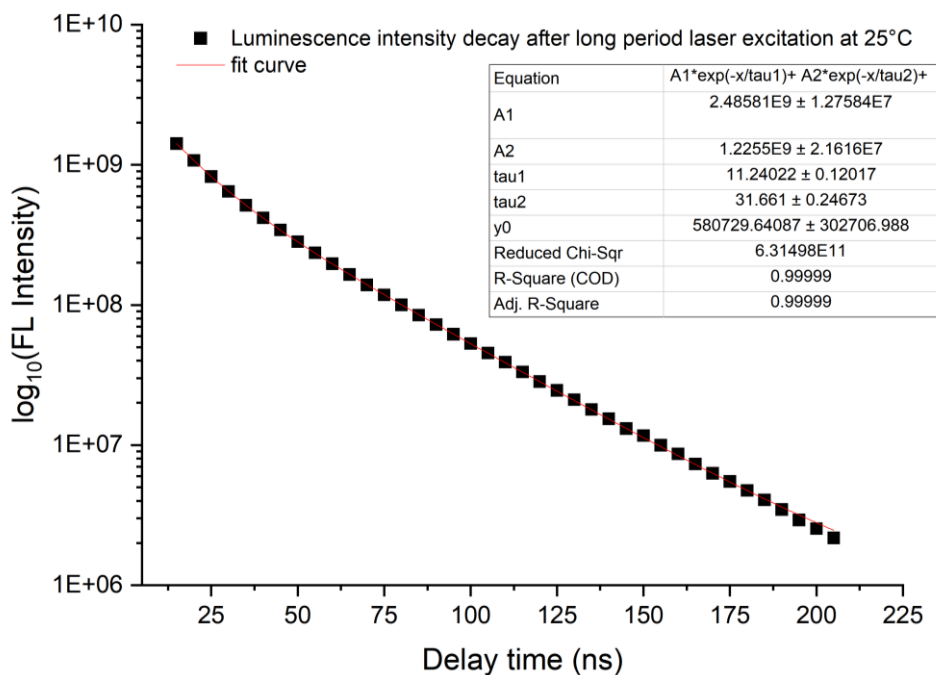
One can note that long period laser excitation at 25°C causes a decrease in the luminescence intensity for the first minor luminescent component 1 with $\tau_1 = (11 \pm 1)$ ns from $A_1 = 7.32 \cdot 10^9$ to $2.49 \cdot 10^9$ while little changes in other parameters, *i.e.* A_2 , τ_1 , τ_2 were observed. Our results suggest that the first minor luminescent component was photolysed due to the laser excitation with static quenching patterns since its decay time did not change. To verify the possible influence of short time fluorescence of organic component, the treated sample was excited at 425, 450, and 470 nm (Figure S11 of the SI). The bands of $\text{Ae}_n\text{UO}_2(\text{CO}_3)_3^{(4-2n)-}$ are apparent whatever the excitation wavelength, but a red-shift of the spectrum with excitation wavelength seems to indicate that the fast component is due to the fluorescence of organic moieties.

Additionally, UV/Vis absorption spectra of the site du Bosc water samples were collected from 200 to 400 nm in order to detect any changes of potentially degraded organic components after laser excitation. As seen in Figure S12 of the SI, the absorption spectra for the original site du Bosc water and the water samples subjected to long period laser excitation of 450 nm at 25

and 50°C are showing subtle differences that are impossible to distinguish using peak decomposition because the values of peak parameters are approximately identical for different spectra taking into account the interval uncertainties. The $E_{254}:E_{204}$ values are also very close, *i.e.* 0.22, 0.21, and 0.22 for untreated water, 5 h laser exposed at 25°C, and 5 h laser exposed at 50°C. Further information on the first minor luminescent complex is difficult to obtain. A decomposition of the spectra allowed identifying at least 3 bands ca. 206, 225, and 239 nm, characteristic of aromatic moieties (Scott, 1964), and which are close to broader peaks decomposed otherwise (Claret et al., 2008; Korshin et al., 1997). The formation of an organic matter uranyl complex under these conditions cannot be ascertained using these experiments, and is considered minor.



a



b

Figure 13. Bi-exponential fits of luminescence intensity decay from $D = 15$ ns to 210 ns for Site du Bosc untreated water (a) before and (b) after long period laser excitation of 450 nm.

Despite that the band positions of the second component correspond most likely to the $\text{Ca}_n\text{UO}_2(\text{CO}_3)_3^{(4-2n)-}$ complexes, the longer lifetime of $\tau_2 = (38 \pm 1)$ ns from the investigated untreated water sample cannot be directly assigned to either $\text{CaUO}_2(\text{CO}_3)_3^{2-}$ or $\text{Ca}_2\text{UO}_2(\text{CO}_3)_3(\text{aq})$. Moreover, distinguishing the $\text{Ca}_n\text{UO}_2(\text{CO}_3)_3^{(4-2n)-}$ complexes based on the band positions is always difficult because of their very similar positions of main emission bands, thus the assignment by characteristic decay time is more tenable. The value of τ_2 is present in the interval of decay times measured for $\text{CaUO}_2(\text{CO}_3)_3^{2-}$ ($\tau \approx 28$ ns) and $\text{Ca}_2\text{UO}_2(\text{CO}_3)_3(\text{aq})$ ($\tau \approx 48$ ns) at $I_m = 0.1$ mol kg_w^{-1} NaCl (Shang and Reiller, 2020). One should note that the decay time of luminescent species is related to the presence of luminescence quenchers in different concentration ratios. Due to quenching effects of chloride, it is reasonable to suppose that $\text{CaUO}_2(\text{CO}_3)_3^{2-}$ should have a longer decay time ($\tau > 28$ ns) in natural and diluted medium, such as in the untreated water sample of $I_m = 0.022$ mol kg_w^{-1} . Therefore, the second lifetime observed for the untreated water sample approaches the characteristic lifetime of $\text{CaUO}_2(\text{CO}_3)_3^{2-}$, indicating a predominance of this species in aqueous solution. The thermodynamic modelling with detailed chemical compositions convincingly verifies this conclusion as 50.6% uranium exists in the form of $\text{CaUO}_2(\text{CO}_3)_3^{2-}$ in the untreated water sample.

4. Conclusion

We have examined the speciation calculation of uranium(VI) in actual situations covering radioactive waste management (RWM), uranium mining activity, and other natural water samples with the previously determined thermodynamic data for $(\text{Mg}/\text{Ca})_n\text{UO}_2(\text{CO}_3)_3^{(4-2n)-}$ complexes in Shang and Reiller (2020, 2021a, b). It represents a comprehensive and the most updated thermodynamic dataset, including the formation constants at infinite dilution $\log_{10}\beta^\circ$, the thermodynamic functions and SIT parameters — specific ion interaction coefficients ε for

$(\text{Mg}/\text{Ca})_n\text{UO}_2(\text{CO}_3)_3^{(4-2n)-}$ complexes —, which can be applied in geochemical calculations covering a wide range of conditions, particularly relevant to nuclear waste disposal.

Based on the repartition of major uranium species obtained in the speciation calculations for the selected water compositions, three ellipsoidal predominance regions of $\text{Ca}_n\text{UO}_2(\text{CO}_3)_3^{(4-2n)-}$ complexes were constructed from the sample point-clouds in $\log_{10}(a(\text{Ca}^{2+})/a(\text{H}^+)^2)$ – $\log_{10}(a(\text{Na}^+)/a(\text{H}^+))$ – $\log_{10}(a(\text{HCO}_3^-)/a(\text{H}^+))$ — and also in $\log_{10}(a(\text{Mg}^{2+})^n a(\text{Ca}^{2+})^{1-n}/a(\text{H}^+)^2)$ – $\log_{10}(a(\text{Na}^+)/a(\text{H}^+))$ – $\log_{10}(a(\text{HCO}_3^-)/a(\text{H}^+))$ — three-dimension spaces. The determination of ellipsoids for $\text{Ca}_n\text{UO}_2(\text{CO}_3)_3^{(4-2n)-}$ complexes allows a quick identification of the major (calcium)carbonatouranyl species for a given natural water sample once its chemical composition is available. Thermodynamic calculations and TRLFS analyses were performed for two water samples collected from the Site du Bosc. The calculated dominant species, i.e. $\text{CaUO}_2(\text{CO}_3)_3^{2-}$, corroborates well the experimental observations in terms of important luminescence characteristics, i.e. band positions and decay time — knowing the lowest emission of $\text{MgUO}_2(\text{CO}_3)_3^{2-}$ in comparison to the $\text{Ca}_n\text{UO}_2(\text{CO}_3)_3^{(4-2n)-}$ species. A minor luminescence species, which decays faster than $(\text{Mg}/\text{Ca})_n\text{UO}_2(\text{CO}_3)_3^{(4-2n)-}$, is suspected to be of a natural organic matter origin, as total organic carbon concentration in the mg_C/L range was measured, and typical patterns of UV-Vis spectrum of aromatic species were detected. The measured luminescent properties for $(\text{Mg}/\text{Ca})_n\text{UO}_2(\text{CO}_3)_3^{(4-2n)-}$ complexes under different conditions — type of electrolyte, ionic strength, and temperature — detailed in preceding works are verified with these sample.

Acknowledgement

This work was financed by ONDRAF-NIRAS (contract DEN4857-CCHO 2018-0456/00/00). Joachim Schick (ORANO) is acknowledged for the shipment of site du Bosc-Lodève water samples.

5. References

- Alkinani M., Kanoua W., Merkel B., 2016. Uranium in groundwater of the Al-Batin alluvial fan aquifer, South Iraq. *Environ. Earth Sci.* 75, 869. <http://doi.org/10.1007/S12665-016-5685-3>.
- Alwan A.K., Williams P.A., 1980. Aqueous chemistry of uranium minerals. Part 2. Minerals of the liebigite group. *Mineral. Mag.* 43, 665-667. <http://doi.org/10.1180/minmag.1980.043.329.17>.
- Baik M.H., Jung E.C., Jeong J., 2015. Determination of uranium concentration and speciation in natural granitic groundwater using TRLFS. *J. Radioanal. Nucl. Chem.* 305, 589-598. <http://doi.org/10.1007/s10967-015-3971-2>.
- Beaucaire C., Toulhoat P., 1987. Redox chemistry of uranium and iron, radium geochemistry, and uranium isotopes in the groundwaters of the Lodève Basin, Massif Central, France. *Appl. Geochem.* 2, 417-426. [http://doi.org/10.1016/0883-2927\(87\)90025-4](http://doi.org/10.1016/0883-2927(87)90025-4).
- Beaucaire C., Michelot J.L., Savoye S., Cabrera J., 2008. Groundwater characterisation and modelling of water–rock interaction in an argillaceous formation (Tournemire, France). *Appl. Geochem.* 23, 2182-2197. <http://doi.org/10.1016/j.apgeochem.2008.03.003>.
- Beccia M.R., Matara-Aho M., Reeves B., Rogues J., Solari P.L., Monfort M., Moulin C., Den Auwer C., 2017. New insight into the ternary complexes of uranyl carbonate in seawater. *J. Environ. Radioact.* 178-179, 343-348. <http://doi.org/10.1016/j.jenvrad.2017.08.008>.

- Bernhard G., Geipel G., Brendler V., Nitsche H., 1996. Speciation of uranium in seepage waters of a mine tailing pile studied by time-resolved laser-induced fluorescence spectroscopy (TRLFS). *Radiochim. Acta* 74, 87-91.
<http://doi.org/10.1524/ract.1996.74.special-issue.87>.
- Bernhard G., Geipel G., Brendler V., Nitsche H., 1998. Uranium speciation in waters of different uranium mining areas. *J. Alloys Compd.* 271, 201-205.
[http://doi.org/10.1016/S0925-8388\(98\)00054-1](http://doi.org/10.1016/S0925-8388(98)00054-1).
- Bernhard G., Geipel G., Reich T., Brendler V., Amayri S., Nitsche H., 2001. Uranyl(VI) carbonate complex formation: validation of the $\text{Ca}_2\text{UO}_2(\text{CO}_3)_3(\text{aq.})$ species. *Radiochim. Acta* 89, 511-518. <http://doi.org/10.1524/ract.2001.89.8.511>.
- Besançon C., Chautard C., Beaucaire C., Savoye S., Sardini P., Gérard M., Descostes M., 2020. The role of barite in the post-mining stabilization of radium-226: a modeling contribution for sequential extractions. *Minerals* 10, 497.
<http://doi.org/10.3390/Min10060497>.
- Bonin B., Blanc P.L., 2001. L'uranium dans le milieu naturel, des origines jusqu'à la mine. In: Métivier H., (Ed.). *L'Uranium, de l'Environnement à l'Homme*. EDP Sciences, Institut de Protection et de Sûreté Nucléaire, Les Ulis, France, in French. pp. 7-41.
- Braz A.M.D., da Costa M.L., Ramos S.J., Dall'Agnol R., Fernandes A.R., 2021. Long term application of fertilizers in Eastern Amazon and effect on uranium and thorium levels in soils. *Minerals* 11, 994. <http://doi.org/10.3390/min11090994>.
- Claret F., Schäfer T., Brevet J., Reiller P.E., 2008. Fractionation of Suwannee River fulvic acid and Aldrich humic acid on $\alpha\text{-Al}_2\text{O}_3$: spectroscopic evidence. *Environ. Sci. Technol.* 42, 8809-8815. <http://doi.org/10.1021/es801257g>.

- Courdouan Merz A., 2008. Nature and Reactivity of Dissolved Organic Matter in Clay Formations Evaluated for the Storage of Radioactive Waste. 7. PhD, ETH Zürich, Zürich, Switzerland, pp. 114. <http://doi.org/10.3929/ethz-a-005680592>.
- Coyte R.M., Jain R.C., Srivastava S.K., Sharma K.C., Khalil A., Ma L., Vengosh A., 2018. Large-scale uranium contamination of groundwater resources in India. Environ. Sci. Technol. Lett. 5, 341-347. <http://doi.org/10.1021/acs.estlett.8b00215>.
- Czerwinski K.R., Buckau G., Scherbaum F., Kim J.I., 1994. Complexation of the uranyl ion with aquatic humic acid. Radiochim. Acta 65, 111-119. <http://doi.org/10.1524/ract.1994.65.2.111>.
- De Craen M., Wang L., Van Geet M., Moors H., 2004. Geochemistry of Boom Clay Pore Water at the Mol site. SCK•CEN-BLG-990, SCK•CEN, Mol, Belgium, pp. 181. http://jongeren.sckcen.be/~media/Files/Science/disposal_radioactive_waste/Geochemistry_of_Boom_Clay_pore_Status_2004.pdf.
- De Vos W., Tarvainen T., Salminen R., Reeder S., De Vivo B., Demetriades A., 2005. FOREGS Geochemical Atlas of Europe, Part 2: Interpretation of Geochemical Maps, Additional Tables, Figures, Maps, and Related Publications: Espoo: Geological Survey of Finland, <http://www.gtk.fi/publ/foregsatlas/>.
- Dong W., Brooks S.C., 2006. Determination of the formation constants of ternary complexes of uranyl and carbonate with alkaline earth metals (Mg^{2+} , Ca^{2+} , Sr^{2+} , and Ba^{2+}) using anion exchange method. Environ. Sci. Technol. 40, 4689-4695. <http://doi.org/10.1021/es0606327>.
- Dong W., Brooks S.C., 2008. Formation of aqueous $MgUO_2(CO_3)_3^{2-}$ complex and uranium anion exchange mechanism onto an exchange resin. Environ. Sci. Technol. 42, 1979-1983. <http://doi.org/10.1021/es0711563>.

- Drozdak J., Leermakers M., Gao Y., Phrommavanh V., Descostes M., 2016a. Novel speciation method based on diffusive gradients in thin films for in situ measurement of uranium in the vicinity of the former uranium mining sites. *Environ. Pollut.* 214, 114-123. <http://doi.org/10.1016/j.envpol.2016.04.004>.
- Drozdak J., Leermakers M., Gao Y., Elskens M., Phrommavanh V., Descostes M., 2016b. Uranium aqueous speciation in the vicinity of the former uranium mining sites using the diffusive gradients in thin films and ultrafiltration techniques. *Anal. Chim. Acta* 913, 94-103. <http://doi.org/10.1016/j.aca.2016.01.052>.
- Emrén A.T., Arthur R., Glynn P.D., McMurry J., 1999. The modeler's influence on calculated solubilities for performance assessments at the Äspö Hard-Rock Laboratory. In: Lee J.H., Wronkiewicz D.J., (Eds). *Scientific Basis for Nuclear Waste Management XXII*. Material Research Society Proceedings. Cambridge University Press. pp. 559-566. <http://doi.org/10.1557/PROC-556-559>.
- Endrizzi F., Rao L., 2014. Chemical speciation of uranium(VI) in marine environments: complexation of calcium and magnesium ions with $[(\text{UO}_2)(\text{CO}_3)_3]^{4-}$ and the effect on the extraction of uranium from seawater. *Chem.-Eur. J.* 20, 14499-14506. <http://doi.org/10.1002/chem.201403262>.
- Endrizzi F., Leggett C.J., Rao L., 2016. Scientific basis for efficient extraction of uranium from seawater. I: understanding the chemical speciation of uranium under seawater conditions. *Ind. Eng. Chem. Res.* 55, 4249-4256. <http://doi.org/10.1021/acs.iecr.5b03679>.
- Fix P.F., 1956. Hydrogeochemical Exploration for Uranium. U.S. Geol. Surv. Prof. Paper 300, 667-672. <http://doi.org/10.3133/pp300>.

- Fox P.M., Davis J.A., Zachara J.M., 2006. The effect of calcium on aqueous uranium(VI) speciation and adsorption to ferrihydrite and quartz. *Geochim. Cosmochim. Acta* 70, 1379-1387. <http://doi.org/10.1016/j.gca.2005.11.027>.
- Gaucher E.C., Tournassat C., Pearson F.J., Blanc P., Crouzet C., Lerouge C., Altmann S., 2009. A robust model for pore-water chemistry of clayrock. *Geochim. Cosmochim. Acta* 73, 6470-6487. <http://doi.org/10.1016/j.gca.2009.07.021>.
- Geipel G., Acker M., Vulpius D., Bernhard G., Nitsche H., Fanghanel T., 2004. An ultrafast time-resolved fluorescence spectroscopy system for metal ion complexation studies with organic ligands. *Spectrochim. Acta A* 60, 417-424. [http://doi.org/10.1016/s1386-1425\(03\)00244-0](http://doi.org/10.1016/s1386-1425(03)00244-0).
- Geipel G., Amayri S., Bernhard G., 2008. Mixed complexes of alkaline earth uranyl carbonates: a laser-induced time-resolved fluorescence spectroscopic study. *Spectrochim. Acta A* 71, 53-58. <http://doi.org/10.1016/j.saa.2007.11.007>.
- Giffaut E., Grivé M., Blanc P., Vieillard P., Colàs E., Gailhanou H., Gaboreau S., Marty N., Madé B., Duro L., 2014. Andra thermodynamic database for performance assessment: ThermoChimie. *Appl. Geochem.* 49, 225-236. <http://doi.org/10.1016/j.apgeochem.2014.05.007>.
- Grenthe I., Gaona X., Plyasunov A.V., Rao L., Runde W.H., Grambow B., Koning R.J.M., Smith A.L., Moore E.E., 2020. Chemical Thermodynamics 14. Second Update on the Chemical Thermodynamics of Uranium, Neptunium, Plutonium, Americium and Technetium. Paris, France: OECD Nuclear Energy Agency Data Bank, Eds., OECD Publications, http://www.oecd-nea.org/jcms/pl_46643/second-update-of-u-np-pu-am-and-tc.

- Grivé M., Duro L., Colàs E., Giffaut E., 2015. Thermodynamic data selection applied to radionuclides and chemotoxic elements: an overview of the ThermoChimie-TDB. *Appl. Geochem.* 55, 85-94. <http://doi.org/10.1016/j.apgeochem.2014.12.017>.
- Grozeva N.G., Radwan J., Beaucaire C., Descostes M., 2022. Reactive transport modeling of U and Ra mobility in roll-front uranium deposits: Parameters influencing $^{226}\text{Ra}/^{238}\text{U}$ disequilibria. *J. Geochem. Explor.* 236, 106961. <http://doi.org/10.1016/j.gexplo.2022.106961>.
- Guillaumont R., Fanghänel T., Fuger J., Grenthe I., Neck V., Palmer D.A., Rand M., 2003. *Chemical Thermodynamics 5. Update on the Chemical Thermodynamics of Uranium, Neptunium, Plutonium, Americium and Technetium.* Amsterdam, The Netherlands: North Holland Elsevier Science Publishers B. V., <http://www.oecd-nea.org/dbtdb/pubs/vol5-update-combo.pdf>; http://www.oecd-nea.org/dbtdb/pubs/Errata_Update.pdf.
- Gurban I., Laaksoharju M., Madé B., Ledoux E., 2003. Uranium transport around the reactor zone at Bangombé and Okélobondo (Oklo): examples of hydrogeological and geochemical model integration and data evaluation. *J. Contam. Hydrol.* 61, 247-64. [http://doi.org/10.1016/s0169-7722\(02\)00131-6](http://doi.org/10.1016/s0169-7722(02)00131-6).
- Hendry M.J., Wassenaar L.I., 2000. Controls on the distribution of major ions in pore waters of a thick surficial aquitard. *Water Resour. Res.* 36, 503-513. <http://doi.org/10.1029/1999WR900310>.
- Hennig T., Stockmann M., Kühn M., 2020. Simulation of diffusive uranium transport and sorption processes in the Opalinus Clay. *Appl. Geochem.* 123, 104777. <http://doi.org/10.1016/j.apgeochem.2020.104777>.

- IAEA, 2001. Manual of Acid in Situ Leach Uranium Mining Technology. TECDOC-1239, IAEA, Vienna, Austria, pp. 283. http://www-pub.iaea.org/MTCD/Publications/PDF/te_1239_prn.pdf.
- IAEA, 2016. Situ Leach Uranium Mining: an Overview of Operations. IAEA, Vienna, Austria. http://www-pub.iaea.org/MTCD/Publications/PDF/P1741_web.pdf.
- Jo Y., Kim H.-K., Yun J.-I., 2019a. Complexation of $\text{UO}_2(\text{CO}_3)_3^{4-}$ with Mg^{2+} at varying temperatures and its effect on U(VI) speciation in groundwater and seawater. Dalton Trans. 48, 14769-14776. <http://doi.org/10.1039/c9dt03313k>.
- Jo Y., Kirishima A., Kimuro S., Kim H.-K., Yun J.-I., 2019b. Formation of $\text{CaUO}_2(\text{CO}_3)_3^{2-}$ and $\text{Ca}_2\text{UO}_2(\text{CO}_3)_3(\text{aq})$ complexes at variable temperatures (10 – 70 °C). Dalton Trans. 48, 6942-6950. <http://doi.org/10.1039/c9dt01174a>.
- Jo Y., Lee J.-Y., Yun J.-I., 2022. Chemical thermodynamics of ternary M-An(VI)- CO_3 system (M = Mg, Ca, Sr, and Ba). Radiochim. Acta. <http://doi.org/10.1515/ract-2021-1133>.
- Kalmykov S.N., Choppin G.R., 2000. Mixed $\text{Ca}^{2+}/\text{UO}_2^{2+}/\text{CO}_3^{2-}$ complex formation at different ionic strengths. Radiochim. Acta 88, 603-606. <http://doi.org/10.1524/ract.2000.88.9-11.603>.
- Kelly S.D., Kemner K.M., Brooks S.C., Fredrickson J.K., Carroll S.L., Kennedy D.W., Zachara J.M., Plymale A.E., Fendorf S., 2005. Ca-UO₂-CO₃ complexation - Implications for bioremediation of U(VI). Phys. Scripta T115, 915-917. <http://doi.org/10.1238/Physica.Topical.115a00915>.
- Kelly S.D., Kemner K.M., Brooks S.C., 2007. X-ray absorption spectroscopy identifies calcium-uranyl-carbonate complexes at environmental concentrations. Geochim. Cosmochim. Acta 71, 821-834. <http://doi.org/10.1016/j.gca.2006.10.013>.
- Kinniburgh D.G., Cooper D.M., 2004. Predominance and mineral stability diagrams revisited. Environ. Sci. Technol. 38, 3641-3648. <http://doi.org/10.1021/es034927l>.

- Kinniburgh D.G., Cooper D.M., 2011. PhreePlot: Creating Graphical Output with PHREEQC: <http://www.phreeplot.org>.
- Korshin G.V., Li C.-W., Benjamin M.M., 1997. Monitoring the properties of natural organic matter through UV spectroscopy: a consistent theory. *Water Res.* 31, 1787-1795. [http://doi.org/10.1016/S0043-1354\(97\)00006-7](http://doi.org/10.1016/S0043-1354(97)00006-7).
- Kubatko K.-A., Helean K.B., Navrotsky A., Burns P.C., 2005. Thermodynamics of uranyl minerals: enthalpies of formation of rutherfordine, UO_2CO_3 , andersonite, $\text{Na}_2\text{CaUO}_2(\text{CO}_3)_3(\text{H}_2\text{O})_5$, and grimselite, $\text{K}_3\text{NaUO}_2(\text{CO}_3)_3\text{H}_2\text{O}$. *Am. Mineral.* 90, 1284-1290. <http://doi.org/10.2138/am.2005.1821>.
- Laaksoharju M., Smellie J., Tullborg E.-L., Gimeno M., Hallbeck L., Molinero J., Waber N., 2008. Bedrock hydrogeochemistry Forsmark. Site descriptive modelling SDM-Site Forsmark. Sweden. <http://www.osti.gov/etdeweb/servlets/purl/951442>.
- Lartigue J.E., Charrasse B., Reile B., Descostes M., 2020. Aqueous inorganic uranium speciation in European stream waters from the FOREGS dataset using geochemical modelling and determination of a U bioavailability baseline. *Chemosphere* 251, 126302. <http://doi.org/10.1016/j.chemosphere.2020.126302>.
- Lee J.-Y., Yun J.-I., 2013. Formation of ternary $\text{CaUO}_2(\text{CO}_3)_3^{2-}$ and $\text{Ca}_2\text{UO}_2(\text{CO}_3)_3(\text{aq})$ complexes under neutral to weakly alkaline conditions. *Dalton Trans.* 42, 9862-9869. <http://doi.org/10.1039/c3dt50863c>.
- Lee J.-Y., Vespa M., Gaona X., Dardenne K., Rothe J., Rabung T., Altmaier M., Yun J.-I., 2017. Formation, stability and structural characterization of ternary $\text{MgUO}_2(\text{CO}_3)_3^{2-}$ and $\text{Mg}_2\text{UO}_2(\text{CO}_3)_3(\text{aq})$ complexes. *Radiochim. Acta* 105, 171-185. <http://doi.org/10.1515/ract-2016-2643>.

- Lee J.-Y., Amayri S., Montoya V., Fellhauer D., Gaona X., Altmaier M., 2019. Solubility and stability of liebigite, $\text{Ca}_2\text{UO}_2(\text{CO}_3)_3 \cdot 10\text{H}_2\text{O}(\text{cr})$, in dilute to concentrated NaCl and NaClO_4 solutions at $T = 22\text{--}80^\circ\text{C}$. *Appl. Geochem.* 111, 104374.
<http://doi.org/10.1016/j.apgeochem.2019.104374>.
- Leggett C.J., Endrizzi F., Rao L., 2016. Scientific basis for efficient extraction of uranium from seawater, II: fundamental thermodynamic and structural studies. *Ind. Eng. Chem. Res.* 55, 4257-4263. <http://doi.org/10.1021/acs.iecr.5b03688>.
- Li B., Zhou J.W., Priest C., Jiang D.E., 2017. Effect of salt on the uranyl binding with carbonate and calcium ions in aqueous solutions. *J. Chem. Phys. B* 121, 8171-8178.
<http://doi.org/10.1021/acs.jpcc.7b04449>.
- Li Y.P., Burns P.C., 2001. The crystal structure of synthetic grimselite, $\text{K}_3\text{Na}[(\text{UO}_2)(\text{CO}_3)_3](\text{H}_2\text{O})$. *Can. Mineral.* 39, 1147-1151.
<http://doi.org/10.2113/gscanmin.39.4.1147>.
- Maia F.M.S., Ribet S., Bailly C., Grivé M., Madé B., Montavon G., 2021. Evaluation of thermodynamic data for aqueous Ca-U(VI)- CO_3 species under conditions characteristic of geological clay formation. *Appl. Geochem.* 124, 104844.
<http://doi.org/10.1016/j.apgeochem.2020.104844>.
- Maloubier M., Solari P.L., Moisy P., Monfort M., Den Auwer C., Moulin C., 2015. XAS and TR-LIF spectroscopy of uranium and neptunium in seawater. *Dalton Trans.* 44, 5417-27. <http://doi.org/10.1039/c4dt03547j>.
- Mereiter K., 1982. The crystal structure of liebigite, $\text{Ca}_2\text{UO}_2(\text{CO}_3)_3 \cdot 11\text{H}_2\text{O}$. *Tschermaks Min. Petr. Mitt.* 30, 277-288. <http://doi.org/10.1007/bf01087173>.
- Meyrowitz R., 1954. Liebigite. In: Frondel C., (Ed.). *Systematic Mineralogy of Uranium and Thorium*. U.S. Geological Survey Bulletin 1064 (1958), Washington. pp. 109-112.

- Meyrowitz R., Ross D.R., Weeks A.D., 1963. Synthesis of liebigite. Geological Survey Professional Paper 475-B, 162-163, <http://pubs.usgs.gov/pp/0475b/report.pdf>.
- Millero F.J., Feistel R., Wright D.G., McDougall T.J., 2008. The composition of standard seawater and the definition of the reference-composition salinity scale. Deep-Sea Res. Pt. I 55, 50-72. <http://doi.org/10.1016/j.dsr.2007.10.001>.
- Montavon G., Ribet S., Hassan Loni Y., Maia F., Bailly C., David K., Lerouge C., Madé B., Robinet J.C., Grambow B., 2022. Uranium retention in a Callovo-Oxfordian clay rock formation: from laboratory-based models to in natura conditions. Chemosphere 299, 134307. <http://doi.org/10.1016/j.chemosphere.2022.134307>.
- Morin J., 2005. Nouveau procédé de traitement des effluents liquides du site de Lodève. Tech. Ind. Miner. 1, 91-96. In French.
- Moulin C., Beaucaire C., Decambox P., Mauchien P., 1990. Determination of uranium in solution at the ng.l^{-1} level by time-resolved laser-induced spectrofluorimetry: application to geological samples. Anal. Chim. Acta 238, 291-296. [http://doi.org/10.1016/S0003-2670\(00\)80550-4](http://doi.org/10.1016/S0003-2670(00)80550-4).
- Nair S., Merkel B.J., 2011. Impact of alkaline earth metals on aqueous speciation of uranium(VI) and sorption on quartz. Aquat. Geochem. 17, 209-219. <http://doi.org/10.1007/s10498-011-9120-9>.
- O'Brien T.J., Williams P.A., 1983. The aqueous chemistry of uranium minerals. 4. Schröckingerite, grimselite, and related alkali uranyl carbonates. Mineral. Mag. 47, 69-73. <http://doi.org/10.1180/minmag.1983.047.342.12>.

- OECD-IAEA, 2014. Uranium 2014: Resources, Production, and Demand. NEA No. 7209, Organization of Economic Cooperation and Development - Nuclear Energy Agency, pp. 504.
[http://inis.iaea.org/collection/NCLCollectionStore/ Public/45/089/45089795.pdf?r=1
&r=1](http://inis.iaea.org/collection/NCLCollectionStore/Public/45/089/45089795.pdf?r=1&r=1).
- Oher H., Vercouter T., Réal F., Shang C., Reiller P.E., Vallet V., 2020. Influence of alkaline earth metal ions (Mg^{2+} and Ca^{2+}) on structures and luminescent properties of $UO_2(CO_3)_3^{4-}$ complex: theoretical and experimental study. *Inorg. Chem.* 59, 15036-15049. <http://doi.org/10.1021/acs.inorgchem.0c01986>.
- Osman A.A.A., Geipel G., Bernhard G., Worch E., 2013. Investigation of uranium binding forms in selected German mineral waters. *Environ. Sci. Pollut. Res.* 20, 8629-8635. <http://doi.org/10.1007/s11356-013-1822-7>.
- Osmond J.K., Cowart J.B., Ivanovich M., 1983. Uranium isotopic disequilibrium in ground water as an indicator of anomalies. *Int. J. Appl. Radiat. Isot.* 34, 283-308. [http://doi.org/10.1016/0020-708X\(83\)90132-1](http://doi.org/10.1016/0020-708X(83)90132-1).
- Parkhurst D.L., Appelo C.A.J., 1999. User's Guide to PHREEQC (Version 2) — A Computer Program for Speciation, Batch-Reaction, One-Dimensional Transport, and Inverse Geochemical Calculations. 99-4259, U.S. Geological Survey, Water-Resources Investigations, Lakewood, Colorado, USA. http://wwwbrr.cr.usgs.gov/projects/GWC_coupled/phreeqci/.
- Parkhurst D.L., Appelo C.A.J., 2013. Description of Input and Examples for PHREEQC Version 3 — A Computer Program for Speciation, Batch-Reaction, One-Dimensional Transport, and Inverse Geochemical Calculations. Chapter 43 of Section A, Groundwater Book 6, Modeling Techniques. U.S. Geological Survey, Denver, Colorado, USA, pp. 497. <http://pubs.usgs.gov/tm/06/a43/pdf/tm6-A43.pdf>.

- Prat O., Vercouter T., Ansoborlo E., Fichet P., Perret P., Kurttio P., Salonen L., 2009. Uranium speciation in drinking water from drilled wells in southern Finland and its potential links to health effects. *Environ. Sci. Technol.* 43, 3941-3946. <http://doi.org/10.1021/es803658e>.
- Priest C., Tian Z.Q., Jiang D.E., 2016. First-principles molecular dynamics simulation of the $\text{Ca}_2\text{UO}_2(\text{CO}_3)_3$ complex in water. *Dalton Trans.* 45, 9812-9819. <http://doi.org/10.1039/c5dt04576b>.
- Ranville J.F., Hendry M.J., Reszat T.N., Xie Q.L., Honeyman B.D., 2007. Quantifying uranium complexation by groundwater dissolved organic carbon using asymmetrical flow field-flow fractionation. *J. Contam. Hydrol.* 91, 233-246. <http://doi.org/10.1016/j.jconhyd.2006.11.002>.
- Reiller P., Moulin C., Beaucaire C., Lemordant D., 1994. Dual use of micellar enhanced ultrafiltration and time-resolved laser-induced spectrofluorometry for the study of uranyl exchange at the surface of alkylsulfate micelles. *J. Colloid Interface Sci.* 163, 81-86. <http://doi.org/10.1006/jcis.1994.1082>.
- Reiller P., 2010. Analyse Critique des Données de Complexation des Lanthanides et Actinides par la Matière Organique Naturelle : Cas des Substances Humiques. Open Report CEA-R-6240 (ISSN 0429-3460), Commissariat à l'Énergie Atomique, Gif-sur-Yvette, France, pp. 184, in French. <http://hal-cea.archives-ouvertes.fr/cea-02285988v1>.
- Reiller P., 2015. Structure-Reactivity Relationships in the Interactions Between Humic Substances, Pollutants from the Nuclear Cycle, and Mineral Surfaces. Open Report CEA-R-6407 (ISSN 0429-3460) Commissariat à l'Énergie Atomique et aux Énergies Alternatives, Gif-sur-Yvette, France, pp. 119. <http://tel.archives-ouvertes.fr/tel-01193077v1>.

- Reiller P., 2022. The PRODATA Thermochemical Database – A Database Applied for Uranium Mining Operations. Open Report CEA-R 6573 (ISSN 0429-3460) Commissariat à l'Énergie Atomique et aux Énergies Alternatives, Gif-sur-Yvette, France, pp. 228. <http://hal-cea.archives-ouvertes.fr/cea-03757400>.
- Reiller P.E., Marang L., Jouvin D., Benedetti M.F., 2012. Uranium (VI) binding to humic substances: speciation, estimation of competition, and application to independent data. In: Merkel B., Schipek M., (Eds). The New Uranium Mining Boom. Challenge and Lessons Learned. Springer-Verlag, Berlin, Germany. pp. 565-572. http://doi.org/10.1007/978-3-642-22122-4_65.
- Reiller P.E., Descostes M., 2020. Development and application of the thermodynamic database PRODATA dedicated to the monitoring of mining activities from exploration to remediation. Chemosphere 251, 126301. <http://doi.org/10.1016/j.chemosphere.2020.126301>.
- Robie R.A., Hemingway B.S., 1995. Thermodynamic Properties of Minerals and Related Substances at 298.15 K and 1 bar (10^5 Pascal) Pressure and at Higher Temperatures. US Geological Survey Bulletin 2131, US Geological Survey, Denver, CO, USA, pp. 461. <http://pubs.usgs.gov/bul/2131/report.pdf>.
- Sachs S., Brendler V., Geipel G., 2007. Uranium(VI) complexation by humic acid under neutral pH conditions studied by laser-induced fluorescence spectroscopy. Radiochim. Acta 95, 103-110. <http://doi.org/10.1524/ract.2007.95.2.103>.
- Salas J., Ayora C., 2004. Groundwater chemistry of the Okélobondo uraninite deposit area (Oklo, Gabon): two-dimensional reactive transport modelling. J. Contam. Hydrol. 69, 115-37. [http://doi.org/10.1016/s0169-7722\(03\)00140-2](http://doi.org/10.1016/s0169-7722(03)00140-2).

Salpeteur I., Angel J.-M., 2010. Valeurs de référence pour les teneurs en éléments traces dans les eaux de rivières et les sédiments, obtenues en France dans le cadre du nouvel Atlas géochimique européen. Environ. Risques Santé 9, 121-135. In French.

<http://doi.org/10.1684/ers.2010.0332>.

Scott A.I., 1964. Interpretation of ultraviolet spectra of natural products. New York, NY, USA: Pergamon Press.

Seigneur N., De Windt L., Déjeant A., Lagneau V., Descostes M., 2021. Long-term evolution of uranium mobility within sulfated mill tailings in arid regions: a reactive transport study. Minerals 11, 1201. <http://doi.org/10.3390/min11111201>.

Shang C., Reiller P.E., 2020. Determination of formation constants and specific ion interaction coefficients for $\text{Ca}_n\text{UO}_2(\text{CO}_3)_3^{(4-2n)-}$ complexes in NaCl solution by time-resolved laser-induced luminescence spectroscopy. Dalton Trans. 49, 466-481.

<http://doi.org/10.1039/C9DT03543E>.

Shang C., Reiller P.E., Vercouter T., 2020. Spectroluminescence measurements of stability constants of $\text{Ca}_n\text{UO}_2(\text{CO}_3)_3^{(4-2n)-}$ complexes in NaClO_4 medium and investigation of interaction effects. Dalton Trans. 49, 15443-15460.

<http://doi.org/10.1039/D0DT03164J>.

Shang C., Reiller P.E., 2021a. Thermodynamic constant of $\text{MgUO}_2(\text{CO}_3)_3^{2-}$ complex in NaClO_4 and NaCl media using time-resolved luminescence spectroscopy, and applications to different geochemical contexts. Dalton Trans. 50, 4363-4379.

<http://doi.org/10.1039/d0dt04124f>.

Shang C., Reiller P.E., 2021b. Effect of temperature on the complexation of triscarbonatouranyl(VI) with calcium and magnesium in NaCl aqueous solution.

Dalton Trans. 50, 17165-17180. <http://doi.org/10.1039/D1DT03204F>.

Smith J.L., 1848. Art. XXXV.—Two new minerals,—Medjidite (sulphate of uranium and lime)—Liebigite (carbonate of uranium and lime). *Am. J. Sci.* 5, 336-338, <http://archive.org/details/mobot31753002152327>.

Smith J.L., 1851. Liebigite. *Am. J. Sci.* 11, 259, <http://archive.org/details/mobot31753002152384>.

Smolíková V., Pelcová P., Ridošková A., Leermakers M., 2022. Diffusive gradients in thin-films technique for uranium monitoring along a salinity gradient: a comparative study on the performance of Chelex-100, Dow-PIWBA, Diphonix, and Lewatit FO 36 resin gels in the Scheldt estuary. *Talanta* 240, 123168. <http://doi.org/10.1016/j.talanta.2021.123168>.

Stetten L., Mangeret A., Brest J., Seder-Colomina M., Le Pape P., Ikogou M., Zeyen N., Thouvenot A., Julien A., Alcalde G., Reyss J.L., Bombled B., Rabouille C., Olivi L., Proux O., Cazala C., Morin G., 2018. Geochemical control on the reduction of U(VI) to mononuclear U(IV) species in lacustrine sediments. *Geochim. Cosmochim. Acta* 222, 171-186. <http://doi.org/10.1016/j.gca.2017.10.026>.

Steutner R., Sachs S., Schmeide K., Brendler V., Bernhard G., 2011a. Ternary uranium(VI) carbonato humate complex studied by cryo-TRLFS. *Radiochim. Acta* 99, 687-692. <http://doi.org/10.1524/ract.2011.1861>.

Steutner R., Müller K., Schmeide K., Sachs S., Bernhard G., 2011b. Binary and ternary uranium(VI) humate complexes studied by attenuated total reflection Fourier-transform infrared spectroscopy. *Dalton Trans.* 40, 11920-11925. <http://doi.org/10.1039/c1dt11089f>.

Stewart B.D., Mayes M.A., Fendorf S., 2010. Impact of uranyl-calcium-carbonato complexes on uranium(VI) adsorption to synthetic and natural sediments. *Environ. Sci. Technol.* 44, 928-934. <http://doi.org/10.1021/es902194x>.

Stockmann M., Fritsch K., Bok F., Marques Fernandes M., Baeyens B., Steudtner R., Müller K., Nebelung C., Brendler V., Stumpf T., Schmeide K., 2021. New insights into U(VI) sorption onto montmorillonite from batch sorption and spectroscopic studies at increased ionic strength. *Sci. Total Environ.* 806, 150653.
<http://doi.org/10.1016/j.scitotenv.2021.150653>.

Thury M.F., Bossart P.J., 1999. Mont Terri Rock Laboratory: Results of the Hydrogeological, Geochemical and Geotechnical Experiments Performed in 1996 and 1997. Geologische Bericht Rapport Géologique Nr. 23, Swiss National Hydrological and Geological Survey, Bern, Switzerland, pp. 234. <http://www.mont-terri.ch/content/mont-terri-internet/en/documentation/publications-from-swisstopo.download/mont-terri-internet/en/publications/publications-swisstopo/GBD-23.pdf>.

Toulhoat P., Beaucaire C., 1993. Géochimie des eaux liées au gisement d'uranium de Cigar Lake (Saskatchewan, Canada) et apport des isotopes de l'uranium et du plomb comme guides de prospection. *Can. J. Earth Sci.* 30, 754-763. In French.
<http://doi.org/10.1139/e93-061>.

Tullborg E.L., Suksi J., Geipel G., Krall L., Auque L., Gimeno M., Puigdomènech I., 2017. The occurrences of $\text{Ca}_2\text{UO}_2(\text{CO}_3)_3$ complex in Fe(II) containing deep groundwater at Forsmark, Eastern Sweden. *Proced. Earth Plan. Sci.* 17, 440-443.
<http://doi.org/10.1016/j.proeps.2016.12.111>.

von Gunten K., Warchola T., Donner M.W., Cossio M., Hao W., Boothman C., Lloyd J., Siddique T., Partin C.A., Lloyd S.L., Rosaasen A., Konhauser K.O., Alessi D.S., 2018. Biogeochemistry of U, Ni, and As in two meromictic pit lakes at the Cluff Lake uranium mine, Northern Saskatchewan. *Can. J. Earth Sci.* 55, 463-474.
<http://doi.org/10.1139/cjes-2017-0149>.

Wang Z.M., Zachara J.M., Yantasee W., Gassman P.L., Liu C.X., Joly A.G., 2004. Cryogenic laser induced fluorescence characterization of U(VI) in Hanford vadose zone pore waters. *Environ. Sci. Technol.* 38, 5591-5597. <http://doi.org/10.1021/Es049512u>.

WHO, 2017. Guidelines for drinking-water quality: fourth edition incorporating first addendum. Geneva, Switzerland: World Health Organization, <http://apps.who.int/iris/handle/10665/254637>.

Yamamoto M., Tomita J., Sakaguchi A., Ohtsuka Y., Hoshi M., Apsalikov K.N., 2010. Uranium isotopes in well water samples as drinking sources in some settlements around the Semipalatinsk Nuclear Test Site, Kazakhstan. *J. Radioanal. Nucl. Chem.* 284, 309-314. <http://doi.org/10.1007/s10967-010-0463-2>.